PHYSICAL REVIEW B **111**, 205419 (2025)

Surface plasmon polaritons in multilayer jellium systems: Dispersion and spatial description

Alexandre Cloots,[1] Tanguy Colleu,[2] Vincent Liégeois,[3] Gian-Marco Rignanese,[1] Luc Henrard,[2] and Xavier Gonze[1,*]

[1]*European Theoretical Spectroscopy Facility, Institute of Condensed Matter and Nanosciences, Université catholique de Louvain, Chemin des étoiles 8, bte L07.03.01, B-1348 Louvain-la-Neuve, Belgium*

[2]*Laboratoire de Physique du Solide, Namur Institute of Structured Matter (NISM), University of Namur, 61, Rue de Bruxelles, B-5000 Namur, Belgium*

[3]*Laboratory of Theoretical Chemistry, Unit of Theoretical and Structural Physical Chemistry, Namur Institute of Structured Matter (NISM), University of Namur, Rue de Bruxelles, 61, B-5000 Namur, Belgium*

(Received 20 December 2024; revised 10 April 2025; accepted 14 April 2025; published 14 May 2025)

Surface-plasmon polaritons (SPPs) are electromagnetic waves that propagate along metal-dielectric interfaces, with important applications in sensing, energy, and nanotechnology. While the behavior of SPPs in single metal slabs is well understood, the coupling between plasmon modes in multilayer systems has received less attention. In this paper, we explore the response functions of SPPs in single-slab, double-slab, and two-different-slab systems using the jellium model. Thanks to a comparison with classical models, in this paper, we reveal how quantum effects influence the resonance frequencies of these modes. We also detail the spatial description of the different SPP modes and unveil how their coupling occurs in two-different-slab systems. These findings provide insights into the behavior of SPPs, especially in complex nanostructures.

DOI: 10.1103/PhysRevB.111.205419

I. INTRODUCTION

Plasmons, which arise from the resonant interaction between electromagnetic fields and electron gases [1,2], have garnered significant attention due to their impact on diverse technological applications. These include enhancing the sensitivity of biosensors [3], improving the efficiency of photovoltaic cells [4], and enabling surface-enhanced vibrational spectroscopies (SEVSs) [5–10]. Plasmonic phenomena are also of particular interest in the field of photonics [11] with, for example, recent advancements in graphene-based plasmonics offering avenues for research [12].

Plasmons can be broadly categorized into two types: volume plasmons, which exist within a bulk material, and surface plasmons, which occur at the interface between a metal and a dielectric medium or vacuum [13]. Surface plasmons, in particular, exhibit unique properties that are especially advantageous for the aforementioned applications. When excited by an external electromagnetic field, surface plasmons result in a pronounced enhancement of the electric field near the material interface, leading to strong field confinement at the nanoscale [5].

Two distinct modes of surface plasmons are typically distinguished: surface-plasmon polaritons (SPPs) and localized surface-plasmon resonances (LSPRs). Both involve the collective oscillation of free electrons within a metal. SPPs are propagating excitations that travel along the interface between a metal and a dielectric, whereas LSPRs are nonpropagating excitations confined at the surface of metallic nanostructures significantly smaller than the wavelength of the incident light [6,13]. In this paper, the focus is on the properties and behavior of SPPs within a jellium model and their implications for plasmonic applications.

The theoretical understanding of SPP phenomena was pioneered by Ritchie [14], who described them using a macroscopic dielectric function approach. Since then, significant advances in both analytical and computational techniques have enabled a more comprehensive characterization of their properties. Early analyses relied on classical electrodynamics, employing Maxwell's equations to describe the electromagnetic fields associated with plasmons [13]. Subsequent developments included the hydrodynamic model, which approximates the electron gas as a fluid, and the jellium model, which provides a simplified treatment of the electron distribution in metals albeit retaining key quantum effects [15–17]. More recently, first-principles calculations have been employed to capture the atomic-scale and quantum mechanical effects underlying plasmon behavior [18].

These theoretical frameworks, ranging from classical to quantum descriptions, have greatly expanded our understanding of plasmon properties [19–24]. A comprehensive overview of these developments up to the early 21st century can be found in the review by Pitarke *et al.* [25].

The jellium model, which approximates a gas of free electrons moving in a uniform, positively charged background, has served as a cornerstone for understanding plasmonic behavior for several decades. This model allows one to focus on the collective electronic properties without the complexities of individual ion cores. While recent advances in computational power have enabled first-principles studies that can now simulate systems containing hundreds of atoms [26–28]—a significant leap compared with the limitations of a few atoms in the past century [29]—the jellium model remains a powerful and insightful tool for many scenarios. It continues to provide valuable insights into various surface and

---

[*] Contact author: xavier.gonze@uclouvain.be

electronic properties, such as the work function [30,31], surface-plasmon-resonance frequencies [14], heterostructure modeling [32], and the behavior of metallic nanospheres [33], all at a significantly lower computational cost than first-principles approaches [34–36].

Besides these successes in providing reasonable results for a wide range of systems, its limitations typically arise only when atomic lattice structures or band-specific effects become prominent. In such cases, more sophisticated adaptations, such as the stabilized jellium model [25,35], the incorporation of empirical atomic layer potentials [37], or advanced screening models tailored for conduction band electrons in materials like silver [38], offer substantial improvements without significantly increasing computational complexity. Thus, the jellium model, along with its modern refinements, is a well-established and valuable framework for exploring and predicting the electronic properties of metals.

Among the different approximations possible to describe the jellium electron gas interactions, the random phase approximation (RPA), discarding the exchange-correlation effect in the density response, is most commonly used. This approximation has long been deemed a decent approach for the prediction of plasmonic phenomena in simple metals such as the alkaline metals [35].

The SPPs that are the focus of this paper are observed experimentally and hence predicted theoretically as peaks in the loss spectra. Their signature can be derived from different approximations, adapted to various experimental situations. Typically, the theory decomposes the interaction of an electron or an electron beam impinging on a surface in excitations in the solid resulting from exchange of given wave vectors and energies. As this electron travels parallel or through the surface, it excites the electron gas, leading to resonant behavior at certain frequencies. Note that a plasmon mode can also be excited by a specific electromagnetic field, provided that the mode and the field together possess the appropriate frequency and spatial characteristics to trigger a resonant behavior. This condition can be met, e.g., by a traveling electron or photon, provided the coupling is adequate.

SPP dispersion relations have long received special attention because they give information about the frequency where a field enhancement can be expected at a given wave vector, which is essential for the proper functioning of applications utilizing plasmonics [21,39–42]. The knowledge of the conditions required to activate a plasmon is indeed a prerequisite to get the signal enhancement at the frequencies of interest as, for example, in SEVS experiments (SERS and SEIRA) and in electron energy loss spectroscopy (EELS) or attenuated total reflection. Various methods have been developed to extract the dispersion relations from the response of the system, including or not the plain bulk effects. In this paper, two distinct approaches to predict the frequencies of SPP modes are considered.

The first is based on the *surface response function* (SRF) as derived by Persson and Zaremba [43]. SRF allows us to predict all the resonance frequencies of surface modes and to obtain a spectrum that can be compared with EELS spectra. This method relies on the density response function. It is worth noting that several similar approaches, relying sometimes on other response functions, have been proposed in the literature to predict results corresponding to different experimental setups [37,44].

A second approach based on the loss function associated with the macroscopic dielectric function, which will be called for the sake of brevity the *macroscopic loss function* (MLF), is also used. The spectrum obtained does not correspond to any experimental setup but to the EELS spectra of a homogeneous material described by the associated effective dielectric function. This common approach in quantum calculations based on the supercell approach also delivers the decomposition into eigenmodes of the dielectric function, which allows for the easy identification of the change of electron density and potential associated with the eigenmodes (and thus characterization of their symmetry) [18]. Similar results can be obtained by directly using the density response function [37].

In this paper, the jellium model is used as a platform to analyze the dispersion of SPPs and their coupling in systems of one or two slabs. The case of a single slab is well established in textbooks using classical methods [13]. Single slabs made of jellium have also been extensively studied. Early publications computed the Fermi energy and work function of such systems [45]. SPP dispersion relations and visualization of collective modes were already found by Dobson [46] and Schaich and Dobson [47]. The single-slab jellium model has since been used to observe the impact of different features of first-principles computations, such as the band structure and exchange-correlation effects [48] or, more recently, to predict EELS spectra [37]. It has also helped to predict a low-energy acoustic plasmon mode in Ag slab systems [49]. First-principles investigations were also performed on single-slab systems for a wide range of materials from Si [50] to Na [18] passing by graphene [51].

At variance, the coupling between surface plasmons in two slabs has been less studied, especially at the quantum level. Results about the van der Waals forces between two slabs have been obtained with the jellium model [36,52], and the dispersion curves of double-slab systems have been predicted using a second-principles method, computationally more efficient than what is presented in this paper but less flexible and yielding less insights about the collective modes [53].

Models that try to incorporate quantum effects in classical approaches have also been used to study these single- and double-slab systems. Among these, the most remarkable ones are those using Feibelman parameters [54] to describe the impact of the electron spill-out and tunneling current [55]. Considering the spill-out, it is possible to match the time-dependent density functional theory results [56]. Feibelman parameters already allowed one to analyze many systems [57]. They were used to characterize the plasmonic response in dimers [58,59]. Using this technique, quantum effects have also been evaluated for layered systems, like those found in this paper [60,61]. A comparison between the jellium approach and the ones using the Feibelman parameters in systems of single and dimer spherical nanoparticles with an emitting point dipole showed that the latter is very accurate except when the dipole is too close from the metallic system [62]. Other models relying on a similar hybrid approach can be found in the literature. For example, the quantum corrected model (where the tunneling is represented by a particular dielectric function where it can occur) has been used to study the impact of quantum effects in a dimer system [63]. The hydrodynamic model has been extended to incorporate nonlocal effects and was able to explain the size-dependent surface resonance shifts in noble metal nanoparticles [64]. Such a model was, however, less accurate for alkaline systems where the jellium model has the reputation to thrive.

The situation where several nanofeatures interact with each other has been well studied, as it occurs more often experimentally. However, the methods above do not explicitly describe the interaction between the plasmon only accessible through a complete quantum description. It is therefore interesting to dig deeper in the understanding of the coupling of the different modes.

In this paper, we rely on a spatial description of the different SPPs to unravel the couplings occurring in double-slab systems. It is important to mention that our numerical tool allows us to study a wide range of systems that can be described by a one-dimensional (1D) potential such as single or multiple slabs.

The methodology is first applied to single slabs as a test case and to position the jellium approach in its RPA form with respect to classical and first-principles approaches. This simple case is also used to identify the strength and failures of the two approaches to predict the frequencies of surface-plasmon modes (SRF and MLF).

Then with these insights, the analysis is extended to a double-slab scenario. The dispersion curves of coupled slabs are extracted, and details about the shape and symmetries of each of the plasmon modes are given, providing in-depth knowledge of the excitation of these systems. Finally, systems consisting of two different slabs are considered, and the conditions to observe a coupling of the plasmonics modes are discussed. We find that the inclusion of quantum effects can lead to energy shifts of the SPP resonant frequency with respect to the classical approximation.

We emphasize that, in this paper, using jellium, we have the transversal goal to clarify and connect the different approaches found in the literature. We also aim to highlight the jellium convenience as an exploratory model. Indeed, this model has a limited interest if one wants to consider other metals than alkaline ones or aluminum. For the latter, it keeps a good predictive capability compared with *ab initio* simulations, as shown hereunder in the case of Na. Nonetheless, it is not a model to be used to design applications: It is a good one to easily access the description of physical interactions, as quantum effects are still considered. Also, its simplicity allows for tackling larger systems, providing insights into those systems out of reach of atomistic methods, such as the multilayer systems mentioned above.

The paper is organized as follows. In Sec. II, the details of the jellium approach are described together with the links with the response functions and the EELS spectra for both the SRF and MLF. In Sec. III, we analyze the case of a single slab, focusing on the main differences between the present jellium model and the classical or first-principles frameworks. Then the coupling of surface-plasmon modes in a double-slab system is considered, with a full description of the dispersion curves for two identical slabs. Afterwards, the two-different-slab case is investigated. The conditions for the coupling of plasmon modes are identified with the description of how this coupling evolves along the dispersion line. In Sec. IV, we summarize our main results. Our computational tool is available on Github [65].

II. THEORY

In this section, we lay the theoretical foundation used to predict the dispersion curves presented in Sec. III. The choice of the potential is first debated. Then the different response functions are presented in the case of systems having two-dimensional (2D) periodicity. Finally, the two approaches (SRF and MLF) to obtain the loss spectra highlighting the collective behavior occurring in such systems are described.

The jellium is uniquely characterized by its electron density n_e or equivalently by the Wigner-Seitz radius r_s [66], which defines the average distance between electrons in the metal. The bulk plasma frequency is given by [66]

$$\omega_\mathrm{p}^2 = 4\pi n_\mathrm{e} = \frac{3}{r_\mathrm{s}^3}. \tag{1}$$

All the equations are given in atomic units [67].

A. Potentials

In this paper, we study systems with translational invariance in the x-y plane. This allows us to reduce the problem to the understanding of what happens along the z direction. The wave functions of these 1D systems $\phi_l(z)$ and their associated energy levels ϵ_l are obtained by diagonalizing the 1D Hamiltonian

$$\hat{H}\phi_l(z) = \left[-\frac{\nabla^2}{2} + V_\mathrm{tot}(z)\right]\phi_l(z) = \epsilon_l\phi_l(z), \tag{2}$$

where $V_\mathrm{tot}(z)$ is a potential representing the system. The energy levels have a parabolic dispersion in the x-y plane. The non-self-consistent field (NSCF) [68] and the self-consistent field (SCF) [30] cases are considered to build the potential. In the first case, the potential of the system is defined *a priori*, while in the second case, a positive background $n^+(z)$ is drawn, and the potential is deduced self-consistently from the joint background profile and the electronic density. In both cases, regions with jellium and regions with vacuum are distinguished, all with x-y translational invariance; the potential has only a z dependence.

Moreover, in this paper, we restrict ourselves to the generic cases of one single slab and two coupled slabs, although the present approach can be adapted to more complex systems with 1D potential. In these generic cases, shown in Fig. 1(a), one assumes that the transition region between the bulk ionic background and the vacuum is infinitely thin. The density of this ionic background is defined to reproduce a neutral material.

Generally speaking, the total potential is composed of four terms:

$$V_\mathrm{tot}(z) = [V(z) + V_\mathrm{Hxc}(z)] + [\delta V_\mathrm{ext}(z) + \delta V_\mathrm{Hxc}(z)]. \tag{3}$$

The first one $V(z)$ is the potential that defines the system under study in the NSCF case. In the SCF case, a second term $V_\mathrm{Hxc}(z)$ is added, the Hartree and exchange-correlation

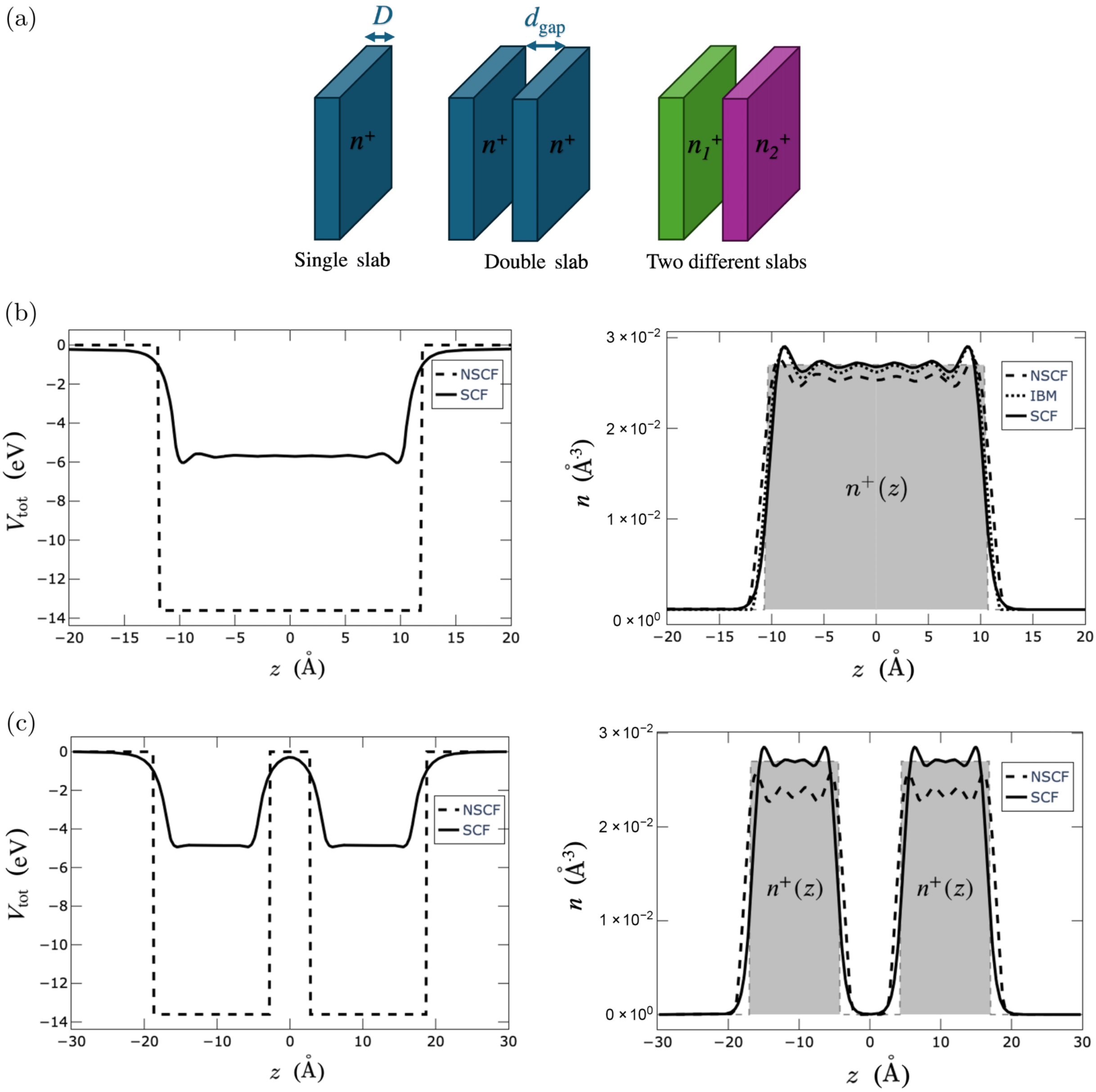

FIG. 1. (a) The three systems studied in this paper: the single slab (left) of width D, the double slab with each slab showing the same width and background density n^+ and being separated by d_{gap} (center), and the two different neutral slabs with the same width but with different background densities (right). (b) The different potentials (left) and their corresponding electronic densities (right) in the case of a single slab reproducing 10 atomic layers of Na. The width is $D = 21$ Å ($n^+ = 0.027$ Å^{-3}). (c) The different models for the potential (left) and their corresponding electronic densities (right) in the case of the double slab each reproducing six atomic layers of Na. The width is $D = 12.6$ Å ($n^+ = 0.027$ Å^{-3}) and $d_{\text{gap}} = 8.47$ Å. The dashed curves correspond to the non-self-consistent-field (NSCF) scenario, and the full curves are the result of the self-consistent-field (SCF) approach.

potential. It is the sum of the Hartree potential

$$V_{\mathrm{H}}(z) = -2\pi \int [n(z') - n^+(z')]|z - z'|dz', \qquad (4)$$

where $n(z)$ is the electronic density profile, and the exchange-correlation potential

$$V_{\mathrm{xc}}(z) = \frac{\delta[e_{\mathrm{xc}}(z)n(z)]}{\delta n(z)}. \qquad (5)$$

The Wigner LDA approximation is chosen for the exchange-correlation energy

$$e_{\mathrm{xc}}(z) = -\frac{0.458}{r_{\mathrm{s}}(z)} + \frac{0.44}{r_{\mathrm{s}}(z) + 7.8}, \qquad (6)$$

where the Wigner-Seitz radius is locally defined as

$$r_{\mathrm{s}}(z) = \left[\frac{3}{4\pi n(z)}\right]^{1/3}. \qquad (7)$$

In the NSCF case, $V_{\mathrm{Hxc}}(z)$ vanishes. In the SCF case, $V(z)$ is used only as a first guess and is then merged with V_{Hxc}

after the first iteration, the latter being the sole nonzero term in V_{tot} at the end of the cycle. The third term $\delta V_{\text{ext}}(z)$ is an external perturbation, which produces a modification of the system. Here, $\delta V_{\text{Hxc}}(z)$ is the variation of the Hartree and exchange-correlation potentials (see later for the corresponding computation) induced by the variation of the density. When the system is perturbed by an applied potential, the response functions include the feedback from the electronic density variation (see Sec. II B).

From the knowledge of the wave functions and relying on the homogeneity and isotropy of the system in the x-y direction, the electronic density $n(z)$ can be calculated as follows [25]:

$$n(z) = \frac{1}{\pi}\sum_i (\epsilon_{\text{F}} - \epsilon_i)|\phi_i(z)|^2\theta(\epsilon_{\text{F}} - \epsilon_i), \tag{8}$$

where ϵ_{F} is the Fermi energy and $\theta(x)$ the Heaviside function. To ensure that the system is neutral, the following criterion is imposed:

$$\int_{-L/2}^{L/2} [n^+(z) - n(z)]dz = 0, \tag{9}$$

where L is the width of the entire system (jellium and vacuum). The nonneutral case has been analyzed by Dobson [24]. Note that the value of the electronic density in Eq. (1) is equal to the average value of the electronic density in the slab $n_{\text{e}} = 1/D \int n(z)dz$.

In the case of the NSCF model, the potential is defined relative to the ionic background profile. For example, in the case of a single slab of width D centered at $z = 0$ (i.e., the background charge spans from $-D/2$ to $D/2$), the potential is defined as follows:

$$V(z) = \begin{cases} 0, & |z| > D/2 + d, \\ C, & |z| < D/2 + d, \end{cases} \tag{10}$$

where C is a negative constant that characterizes the jellium with respect to the vacuum. Its value will impact the spill-out of the electrons from the jellium to the vacuum. In a neutral system, $d = (\frac{3}{16})\lambda_{\text{F}}$, with λ_{F} the Fermi wavelength directly linked to the Wigner-Seitz radius, can be considered a reasonable value to realistically account for the range of the spill-out of the electronic gas. In the case of a double-slab system, the single-slab potential is duplicated leaving a space d_{gap} between the two wells.

In the case of the SCF model, the potential $V(z)$ is chosen as an initial guess $V^0_{\text{tot}}(z)$. Then Eq. (8) is used to calculate the initial density $n^0(z)$. To get a matching density-potential pair, a self-consistency cycle is started whereby, at the iteration $j + 1$, the potential $V^{j+1}_{\text{tot}}(z)$ is calculated from the density $n^j(z)$, and the density $n^{j+1}(z)$ is obtained using the potential $V^{j+1}_{\text{tot}}(z)$ in Eq. (8), until they meet that requirement. To avoid any convergence issues in the SCF cycle, we rely on a simple mixing algorithm with a preconditioner in which the potential is updated as follows [69]:

$$V^{j+1}_{\text{tot}}(z) = V^j_{\text{tot}}(z) + \int \varepsilon^{-1}(z, z') \times \{V_{\text{Hxc}}[n^j](z') - V^j_{\text{tot}}(z')\}dz', \tag{11}$$

The preconditioner $\varepsilon^{-1}(z, z')$ is the fully periodic, static value of the inverse dielectric function $\varepsilon^{-1}(z, z'; q = 0, \omega = 0)$, which is defined in the next subsection [Eq. (16)].

Figure 1 illustrates the two potential models (NSCF and SCF) with their associated densities. Figure 1(b) illustrates the single-slab scenario, while Fig. 1(c) shows the double-slab case.

Another usual model found in the literature is the infinite barrier model (IBM), in which the C parameter of our NSCF approach is set equal to $-\infty$. The SCF and IBM density profiles [the latter is also shown in Fig. 1(b) for a single-slab case, for information] are very similar, but the SCF and IBM potentials are very different, as the vacuum is not accessible for the electrons in the second case, making the excitations (electron-hole and plasmons) not correctly predicted. This justifies the choice of a NSCF potential with an adjustable depth (C parameter). It allows one to tune the spill-out and work function to better match the SCF results.

B. Response functions

Different response functions can be defined to analyze the SPP excitations of surfaces and slabs. Those functions describe the response of the system to an external perturbation. For example, the perturbation can be a time-dependent electric field, resulting in a time-dependent modification of the charge density. The irreducible (or *noninteracting*) density response links the total variation of the potential at point z' to the total variation of charge density at coordinate z. It has been obtained by Eguiluz [70] for Hartree electrons (so not considering exchange and correlation), for systems having a 2D periodicity [71]

$$\begin{aligned}\chi^0(\mathbf{q}_{||}, \omega; z, z') &= \frac{\delta n_{\text{tot}}(\mathbf{q}_{||}, \omega; z)}{\delta V_{\text{tot}}(\mathbf{q}_{||}, \omega; z')} \\ &= \sum_{l=1}^{l_M}\sum_{l'=1}^{\infty} F_{ll'}(\mathbf{q}_{||}, \omega)\phi_l(z) \\ &\quad \times \phi_{l'}(z)^*\phi_l^*(z')\phi_{l'}(z'),\end{aligned} \tag{12}$$

where l and l' are the different electronic subbands of the slab and $\mathbf{q}_{||}$ the wave vector of the perturbation parallel to the surface, so in the x-y plane. Here, l_M is the maximum occupied subband of the slab. The $F_{ll'}$ factor is defined as

$$F_{ll'}(\mathbf{q}_{||}, \omega) = -\frac{1}{A}\sum_{\mathbf{k}_{||}} f_{\mathbf{k}_{||}l}\left[\frac{1}{\mathbf{q}_{||}\cdot\mathbf{k}_{||} + a_{ll'}(\mathbf{q}_{||}) + \omega + i\eta} + \frac{1}{\mathbf{q}_{||}\cdot\mathbf{k}_{||} + a_{ll'}(\mathbf{q}_{||}) - \omega - i\eta}\right], \tag{13}$$

where $f_{\mathbf{k}_{||}l}$ is the Fermi-Dirac filling of a given state for a given $\mathbf{k}_{||}$, a reciprocal vector parallel to the surface of the slab [72], A the area of the surface of the slab, and

$$a_{ll'}(q_{||}) = \frac{q_{||}^2}{2} - (\epsilon_l - \epsilon_{l'}), \tag{14}$$

with $q_{||} = |\mathbf{q}_{||}|$. In the present case, since $\mathbf{q}_{||}$ is defined in the x-y plane where there is a rotational (and translational) invariance and since the sum over $k_{||}$ in Eq. (13) can be replaced by a factor $2A(\epsilon_\mathrm{F} - \epsilon_l)/(2\pi)$, the response function can be expressed as a function of the norm of the wave vector.

The irreducible density response function being computed, one can obtain the dielectric function ε as well as its inverse [already used as a preconditioner in Eq. (11)]. Both quantities ε and ε^{-1} link the external perturbation δV_ext to the variation of the total potential δV_tot in the system. The subscript "ext" indicates that it is purely the applied variation, while the "tot" one also considers the reaction from the system. It is the total difference of the potential in the system after and before the perturbation is applied.

The dielectric function is defined as

$$\begin{aligned}\varepsilon(z, z'; q_{||}, \omega) &= \frac{\delta V_\mathrm{ext}(q_{||}, \omega; z)}{\delta V_\mathrm{tot}(q_{||}, \omega; z')} \\ &= \delta(z - z') - \int dz''\{v_\mathrm{c}(z, z''; q_{||}) + f_\mathrm{xc}[n_0] \\ &\quad \times (z, z''; q_{||}, \omega)\}\chi^0(z'', z'; q_{||}, \omega), \end{aligned} \tag{15}$$

and its inverse as

$$\begin{aligned}\varepsilon^{-1}(z, z'; q_{||}, \omega) &= \frac{\delta V_\mathrm{tot}(q_{||}, \omega; z)}{\delta V_\mathrm{ext}(q_{||}, \omega; z')} \\ &= \delta(z - z') + \int dz''\{v_\mathrm{c}(z, z''; q_{||}) + f_\mathrm{xc}[n_0] \\ &\quad \times (z, z''; q_{||}, \omega)\}\chi(z'', z'; q_{||}, \omega), \end{aligned} \tag{16}$$

where $v_\mathrm{c}(z, z'; q_{||})$ is the Coulomb potential, and $f_\mathrm{xc}[n_0] = \frac{\delta V_\mathrm{xc}[n]}{\delta n}|_{n=n_0}$, the exchange-correlation kernel, where n_0 is the unperturbed density.

In the particular geometry considered here, with planar translational invariance, the Coulomb potential is obtained as the inverse Fourier transform on the q_z component of the three-dimensional (3D) potential

$$v_\mathrm{c}(z, z'; q_{||}) = \frac{2\pi}{q_{||}} \exp[-q_{||}|z - z'|]. \tag{17}$$

It reduces to the $q_{||} = 0$ limit, and $v_\mathrm{c} = |z - z'|$ if the charge neutrality is considered, as in Eq. (4).

The reducible density response function χ is obtained by means of a Dyson equation

$$\begin{aligned}\chi(z, z'; q_{||}, \omega) &= \frac{\delta n_\mathrm{tot}(q_{||}, \omega; z)}{\delta V_\mathrm{ext}(q_{||}, \omega; z')} \\ &= \chi^0(z, z'; q_{||}, \omega) + \int dz_1 \int dz_2 \chi^0 \\ &\quad \times (z, z_1; q_{||}, \omega)\{v_\mathrm{c}(z_1, z_2, q_{||}) + f_\mathrm{xc} \\ &\quad \times [n_0](z_1, z_2; q_{||}, \omega)\}\chi(z_2, z'; q_{||}, \omega). \end{aligned} \tag{18}$$

It will be denoted as Hxc reducible response if both the Coulomb and the exchange-correlation are integrated into the equation. If one applies the RPA in which the exchange-correlation kernel vanishes $f_\mathrm{xc}[n_0] = 0$, the resulting function is called the *interacting* density response function.

Finally, the screened interaction W gives the change of total potential at z induced by an external charge at z',

$$\begin{aligned}W(z, z'; q_{||}, \omega) &= \frac{\delta V_\mathrm{tot}(q_{||}, \omega; z)}{\delta n_\mathrm{ext}(q_{||}, \omega; z')} \\ &= v_\mathrm{c}(z, z'; q_{||}) + \int dz_1 \int dz_2 v_\mathrm{c}(z, z_1; q_{||}) \\ &\quad \times \chi(z_1, z_2; q_{||}, \omega) v_\mathrm{c}(z_2, z'; q_{||}). \end{aligned} \tag{19}$$

This set of equations was implemented numerically in the matrix formalism (where the rows and columns of the matrix correspond to the z coordinates). In the RPA ($f_\mathrm{xc} = 0$), Eq. (15) for a given $(q_{||}, \omega)$ becomes

$$\underline{\varepsilon} = \underline{\mathbf{I}} - \underline{\mathbf{v}}_\mathrm{c}\underline{\chi}^\mathbf{0}. \tag{20}$$

The inverse dielectric function is obtained by inverting this matrix. A numerically stable way to compute the reducible density response function is to extract it from the right-hand side of Eq. (16):

$$\underline{\chi} = \underline{\mathbf{v}}_\mathrm{c}^{-1}(\underline{\varepsilon}^{-1} - \underline{\mathbf{I}}). \tag{21}$$

Finally, the screened interaction from Eq. (19) is computed as

$$\underline{\mathbf{W}} = \underline{\mathbf{v}}_\mathrm{c} - \underline{\mathbf{v}}_\mathrm{c}\underline{\chi}\underline{\mathbf{v}}_\mathrm{c}. \tag{22}$$

In the case where the wave functions and energies are computed based on the SCF potential, this algorithm to obtain the response functions is called *SCF-based RPA*.

C. SRF

In this section, we present a first approach to obtain loss spectra. It is more closely related to an experimental setup than the one using the macroscopic dielectric function, presented in Sec. II D. The justification of the use of the two methods is that the first method leads to a good understanding of the system based on actual experimental setups and focusing on the surface mode. The second method allows one to better characterize the modes found in the first method, irrespectively of the experimental setup (see Sec. II D).

The SRF allows one to extract a spectrum like the one obtained in an EELS experiment. It evaluates the loss of energy of an electron traveling close to a surface, losing quanta of energy, mainly by exciting the associated plasmon. The SRF $[g(q_{||}, \omega)]$ can be computed from the interacting density response functions defined in the previous section. It is given by [25]

$$\begin{aligned}g(q_{||}, \omega) = -\frac{2\pi}{q_{||}} \int dz_1 \int dz_2 \exp[q_{||}(z_1+z_2)] \\ \times \chi(z_1, z_2; q_{||}, \omega). \end{aligned} \tag{23}$$

The screened interaction of Eq. (19) for coordinates $z, z' > 0$ and far from the surface (so where the electronic density is null) can, in this case, be expressed as a function of this SRF [44]

$$\begin{aligned}W(z, z'; q_{||}, \omega) &= v_\mathrm{c}(z, z', q_{||}) \\ &\quad - \frac{2\pi}{q_{||}} \exp[-q_{||}(z + z')]g(q_{||}, \omega). \end{aligned} \tag{24}$$

The rate at which the external potential generates electronic excitation in the many-body system is defined from Fermi's golden rule

$$w(\omega) = 2\pi \sum_{\mathbf{k},\mathbf{k}'} f_{\mathbf{k}}(1 - f_{\mathbf{k}'})|\langle \mathbf{k}'|V_{\text{tot}}|\mathbf{k}\rangle|^2 \delta(\epsilon_{\mathbf{k}} - \epsilon_{\mathbf{k}'} - \omega). \tag{25}$$

This rate can be related to the response functions thanks to [35]

$$w(\omega) = -2\,\text{Im} \int d^3r V^*_{\text{ext}}(\mathbf{r}, \omega)\delta n(\mathbf{r}, \omega). \tag{26}$$

Using the response functions above and with an external potential of the shape [35]

$$V_{\text{ext}}(\mathbf{q}_{||}, \mathbf{r}) = -\frac{2\pi}{q_{||}} \exp(i\mathbf{q}_{||} \cdot \mathbf{r}_{||}) \exp(q_{||}z), \tag{27}$$

which describes the field generated by a charged particle traveling far from the surface in the $z > 0$ region, and it reduces to

$$w(q_{||}, \omega) = \frac{4\pi}{q_{||}A} \text{Im}\, g(q_{||}, \omega). \tag{28}$$

Hence, the peaks in the imaginary part of the SRFs are associated with both one electron and collective excitations. This function can be compared with the results of an EELS experiment, as the resonances in both cases are associated to the electron energy loss.

The EELS spectra can also be computed for perpendicular or parallel trajectories of the electrons from the screened interaction response function or the reducible density response function, as detailed in Echarri *et al.* [37] or Garcia-Lekue and Pitarke [44]. Here, we limit ourselves to the study of the imaginary part of the screened interaction for $z = z'$ and the SRF, as they comprise the leading term to predict EELS spectra, and we are not comparing our results with a specific experimental result. The aim is rather to gather spatial information about the plasmon mode. Note that, for the simulation of an EELS spectrum, the response is analyzed at the electron position ($z = z'$) and that this position can be inside the slab as well as outside the slab. In the latter case, only the SPP is excited, while in the former case, volume plasmon dominates. The analysis of $\text{Im}\, W(z_0, z; q_{||}, \omega)$ for a z_0 close to the surface [73] allows one to highlight the symmetries of the surface mode, which is not possible if only the $z = z'$ response function is known. The use of the screened interaction function to obtain the spatial description of the modes is then less straightforward (it does not show all the modes and symmetries at once) than the one proposed in Sec. II D.

D. MLF

The second approach used in this paper is the computation of the MLF. As stated earlier and contrary to the previous section, this function does not correspond directly to any experimental geometry. Nonetheless, this approach is interesting to acquire a better understanding of the different plasmon modes involved, as the spatial density change can be described easily. The macroscopic dielectric function (spatial average of the dielectric function, hence considering the vacuum in the cell in our case) is the basic quantity to extract the relevant information. Indeed, it is well known that plasmon modes occur at the poles of $\varepsilon_{\text{M}}^{-1}(q, \omega)$, i.e., where the real part of the dielectric function is small. It is also the quantity that is commonly extracted from *ab initio* simulations of a slab, in a supercell geometry.

To obtain a spatial representation of each mode, Andersen *et al.* [18] relied on the spectral representation of the dielectric function, which reads, in mixed space $(q_{||}, z)$ [18],

$$\varepsilon(z, z'; q_{||}, \omega) = \sum_i \varepsilon_i(q_{||}, \omega)V_i(z; q_{||}, \omega)\rho^*_i(z'; q_{||}, \omega). \tag{29}$$

The index i labels the different eigenpotential-eigendensity pairs (V_i, ρ_i) and the associated eigenvalue ε_i. They propose an algorithm that uses the fact that collective oscillations are associated with poles of the inverse dielectric function eigenvalues ε_i^{-1}, and therefore, the maxima of $\text{Im}\,\varepsilon_i^{-1}(q, \omega)$ describe plasmon resonances characterized by the electronic density ρ^*_i.

The dielectric function can alternatively be expressed in reciprocal space. Indeed, since the supercell formalism is being used to perform the computations (the supercell is made of jellium and vacuum), it gives equivalently [74,75]

$$\varepsilon_{G,G'}(q_{||}, \omega) = \sum_i \varepsilon_i(q_{||}, \omega)V_{i,G}(q_{||}, \omega)\rho^*_{i,G'}(q_{||}, \omega), \tag{30}$$

where G and G' are the 1D reciprocal vectors along the z direction.

The MLF, denoted L_{M}, gives the loss incurred by electrons traveling in an hypothetical homogeneous medium described by ϵ_M. The MLF is defined as

$$L_{\text{M}}(q_{||}, \omega) = -\text{Im} \frac{1}{\varepsilon_{\text{M}}(q_{||}, \omega)}. \tag{31}$$

The difference with the approach of the previous section is that the geometry of the system is not correctly described. It is therefore not possible to connect the spectrum to an experimental setup.

The macroscopic dielectric function ε_{M} is the spatial average of the microscopic dielectric function (it is taken as the inverse of the constant component of the inverse dielectric function to include the local effects)

$$\varepsilon_{\text{M}} = \frac{1}{\varepsilon^{-1}_{G=0,G'=0}(q_{||}, \omega)}. \tag{32}$$

It can be decomposed in a weighted sum of its eigenmodes

$$\begin{aligned} L_{\text{M}}(q_{||}, \omega) &= -\text{Im} \sum_i w_i \frac{1}{\varepsilon_i(q_{||}, \omega)} \\ &= \sum_i w_i(q_{||}, \omega)L_i(q_{||}, \omega), \end{aligned} \tag{33}$$

with

$$w_i(q, \omega) = V_{i,G=0}(q, \omega)\rho^*_{i,G=0}(q, \omega), \tag{34}$$

$$L_i(q_{||}, \omega) = -\text{Im} \frac{1}{\varepsilon_i(q_{||}, \omega)}. \tag{35}$$

Since the macroscopic quantities presented above are spatial averages of their microscopic counterparts, the response functions should be renormalized to compare results obtained with different supercell sizes [76,77].

This algorithm then gives a global view of the plasmonic response and, thanks to its decomposition in eigenmodes, allows one to visualize the spatial variation of each mode through the eigenvector $V_i(z, q_{||})$ and $\rho_i(z, q_{||})$.

It can already be noted that the surface response and the MLF spectrum do not present the same peak intensities. Indeed, the weights used in the construction of the macroscopic loss are zero in the case of antisymmetric modes. However, those modes are also associated with a field enhancement in the vicinity of the surface. On the other hand, the decomposition in eigenmodes used in the build-up of the loss function allows one to retrieve the spatial description of all the modes (symmetric and antisymmetric alike). This information is complementary and alleviates the need to use paired and unpaired wave functions in two sets as in Ref. [42].

E. Numerical parameters

The results in the following section were obtained using a grid of points along the z direction with a spacing ranging from 0.18 to 0.5 Å and with 40–120 Å of vacuum, depending on the system under study (the larger the parallel wavelength, the larger the vacuum; the smaller the wavelength, the smaller the grid spacing). The damping parameter η in Eq. (13) was fixed to 0.05 eV. Convergence with respect to the number of unoccupied bands was performed to guarantee an accuracy of 0.02 eV on the position of any plasmon peak position. The background density corresponds to the electronic density of Na, $n^+ = 0.004$ Bohr^{-3} $= 0.027$ Å^{-3}. The height of the barrier in the NSCF was set to 0.5 Ha = 13.61 eV. It was chosen to reproduce as well as possible the plasmonic modes found with the SCF potential in the single-slab case. A smaller height, closer to the experimental value of sum of the Fermi level and the work function, led to a redshift of the mode, while a larger value, closer to what one would use in the IBM case, led to a blueshift of the surface peak, as the energy levels of the vacuum are not accessible. Throughout this paper, the self-consistent potential and density profiles were obtained after 5–10 cycles [convergence was considered achieved when $\frac{1}{L}\int |n_{i+1}(z) - n_i(z)| dz < 10^{-7}$ Bohr^{-3} $\approx 10^{-6}$ Å^{-3}].

III. RESULTS AND DISCUSSION

A. Single slab

In this section, we explore the dielectric properties and collective excitations of a simple jellium slab model, considering both NSCF and SCF potentials. The differences between these approaches and their impact on the resulting dispersion relations are analyzed. The reference system aims at reproducing a 10 layer Na slab (surface with normal vector [001]) and is shown in Fig. 1(b). We use the first-principles value of 21 Å [18] for the width of the slab (D).

As illustrated in the left part of Fig. 1(b), the ground-state electron density profiles for the two scenarios exhibit similar behavior within the slab, showing Friedel oscillations [47,78] in both cases, but differ outside the surface with a more pronounced spill-out of the electrons in the NSCF case. The SCF potential, on the other hand, is very different from the NSCF one, as shown on the left part of Fig. 1(b). The height of the barrier in the SCF case (=4.86 eV) is closer to the sum of the real work function (experimental value ≈2.25 eV [79], computed 1.49 eV) and real Fermi level (experimental value ≈3.24 eV [80], computed 3.36 eV) than in the NSCF case, where the height was set to 13.61 eV. As mentioned above, this value was chosen to get the right position of the surface-plasmon peaks. Using a more realistic value for the work function in NSCF leads to a redshift of the peak positions. Additionally, some ripples mimicking the Friedel oscillations of the density can be seen at the bottom of the SCF potential which, by construction, are not present in the NSCF case.

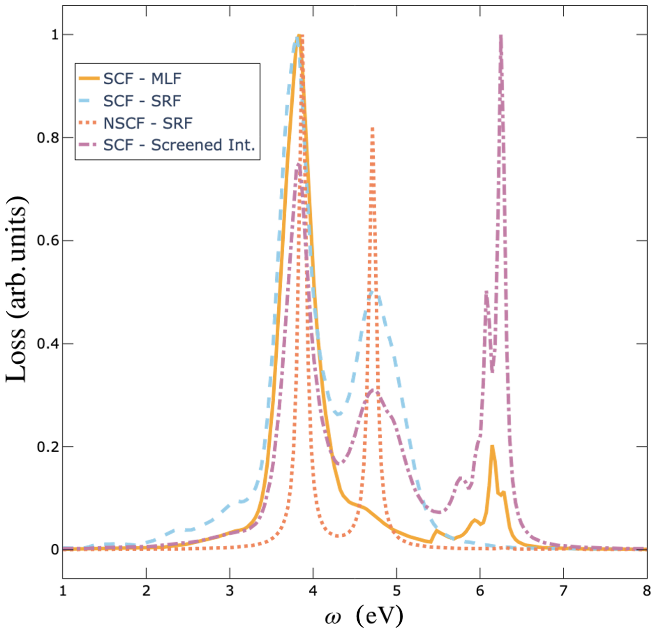

FIG. 2. Four spectra of energy losses. Three are from the two methodologies [macroscopic loss function (MLF) and surface response function (SRF)], with a comparison between the non-self-consistent-field (NSCF) and self-consistent-field (SCF) potentials, and one is obtained from screened interaction function. The spectra are shown for $q_{||} = 0.076$ Å^{-1}. The spectrum for the NSCF case extracted from the SRF is in dotted coral, with two surface modes at 3.87 and 4.71 eV and one bulk mode (much less intense) at 6.29 eV. The spectra found with the SCF approach are in solid line orange in the case of the MLF, showing one surface mode at 3.83 eV and the bulk mode at 6.16 eV, and in dashed light blue in case of the SRF, showing two surface modes (3.80 and 4.71 eV). In the latter case, the bulk mode is not seen on the figure. The spectrum obtained as the sum over all z of the screened interaction $\sum_z \mathrm{Im}\, W(z, z; \omega)$ is in dot-dashed purple.

Figure 2 presents spectra obtained for $q_{||} = 0.076$ Å: with SCF approach or not, SRF, MLF, or with the screened interaction function (performing a sum over all $z = z'$ positions at each frequency). In those spectra, three main peaks can be identified. The two peaks with the lowest energy ∼3.83 and 4.71 eV are attributed to the SPP, while the third one ∼6.2 eV (only visible with the MLF and the screened interaction methods) is a bulk plasmon. This identification is substantiated

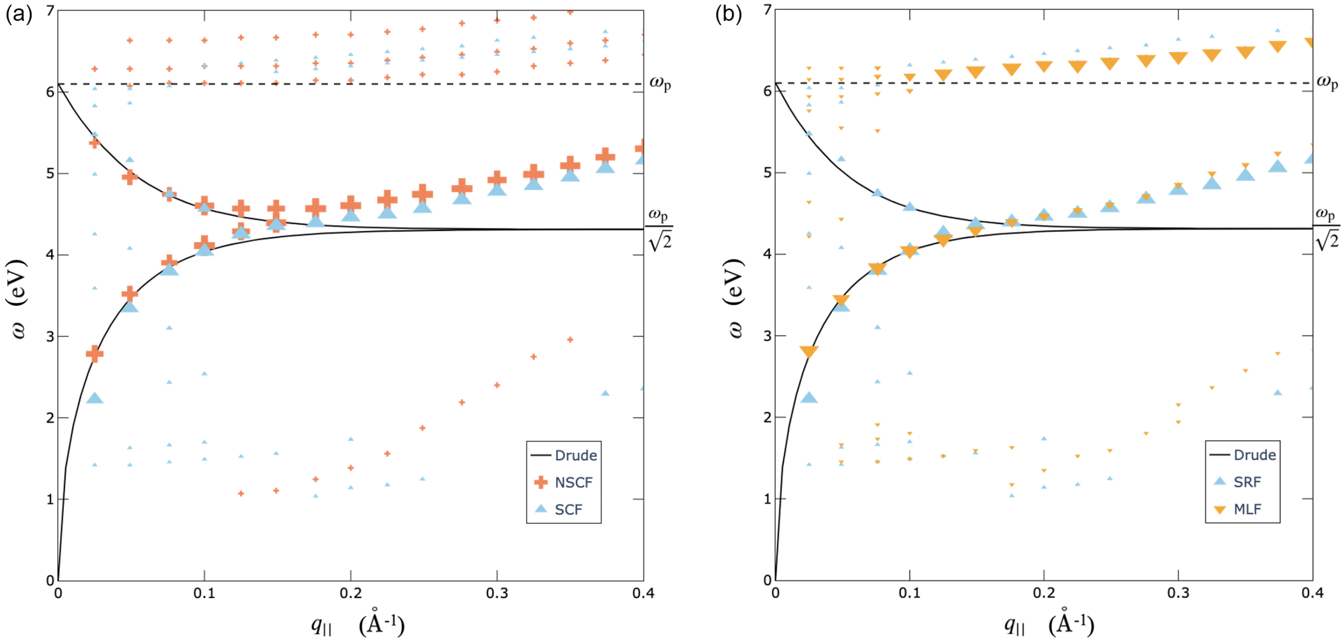

FIG. 3. Dispersion relations obtained in the jellium model [non-self-consistent field (NSCF) and self-consistent field (SCF)] with random phase approximation (RPA) compared with those obtained in the classical case with the Drude model as an approximation for $\varepsilon(\omega)$, for a slab equivalent to a 10-layer system of Na ($D = 21$ Å). The size of the markers is proportional to the relative intensity of the peak with respect to the highest one of each spectrum (one per $q_{||}$). (a) Comparison of the peaks found in the surface response functions (SRFs) for the NSCF model with a potential following Eq. (10) (coral) and for the SCF model (light blue). (b) Comparison of the peaks found in the macroscopic loss function (MLF; orange) and SRF (blue), both for the SCF model.

hereafter. Note that the spectra have been normalized to the maximum of the functions. A significant difference between the MLF and SRF spectra is the near disappearance of the second SPP peak in the former (only a shoulder in the first peak is visible). The second SPP peak in the SRF spectra can therefore be attributed to an asymmetric mode, as explained in Sec. II and as corroborated by the visualization of the mode hereafter. The range of frequency close to the plasma frequency also highlights typical differences between the spectra. In the SRF, the bulk plasmon appears very weak, as this function monitors the induced fields outside the slab. In the MLF and screened interaction spectra, the bulk plasmon peak is subdivided into two bulk modes (6.07 and 6.25 eV) which are preceded by a weak subsurface mode ∼5.8 eV. After checking that the screened interaction yields the same peak positions as the other methodologies, we infer that all the information required to perform the rest of our analysis are contained in the SRF and MLF methodology.

The two density profiles (NSCF and SCF), even with different tails outside the surface, lead to the emergence of similar surface modes, as already found by Echarri *et al.* [81] and in stark contrast with the hydrodynamic mode where these details matter much more [82]. Figure 3(a) compares the dispersion relations obtained from the SRF for the two potentials [in the SCF case, the RPA, Eqs. (20)–(22), was used at the level of the response function] with those of the classical approach of dielectric continuum with a Drude model for the response function with $\omega_p = 6.10\,\text{eV}$. The dispersion relations show the peaks in the spectra, as illustrated in Fig. 2. Note that two resonances cannot be distinguished when they are very close compared with the width of the excitations.

The Drude model uses a simple dielectric function [13]

$$\varepsilon(\omega) = \varepsilon_0\left(1 - \frac{\omega_p^2}{\omega^2}\right) \tag{36}$$

and yields the following dispersion relation for a single slab:

$$\omega_\pm^2(q_{||}) = \tfrac{1}{2}\omega_p^2[1 \pm \exp(-q_{||}D)]. \tag{37}$$

This model gives two surface plasmons. The first one [the − sign in Eq. (37)] has the same symmetry as the slab; the second one [the + sign in Eq. (37)] is an antisymmetric mode. From Fig. 3(a), it is evident that both SCF and NSCF approaches result in dispersion curves very close to the dielectric model in the long-wavelength limit, with a remarkable agreement up to $q_{||} = 0.15$ Å^{-1}. The main differences between the two approaches are (i) the intensity of the bulk mode is not very weak by the SRF, and (ii) weak electron-hole excitation continuum, lacking in the dielectric model, is observed in the jellium model at the lower energy region (<3 eV) and for intermediate wavelength (0.1 Å^{-1} $< q_{||} <$ 0.4 Å^{-1}; Fig. 3). The peaks of these excitations are, however, several orders of magnitude weaker than the peaks of the SPP modes, leading to transfer of far less energy. We also note that the symmetric and antisymmetric SPPs merge at large momentum transfer in all the approach because of the decoupling of the surface modes due to the rapid decrease of the electric field.

Figure 3(b) contrasts dispersion spectra obtained from the SRF and MLF. It has already been noted that the antisymmetric mode is very weak in the MLF approach as a consequence

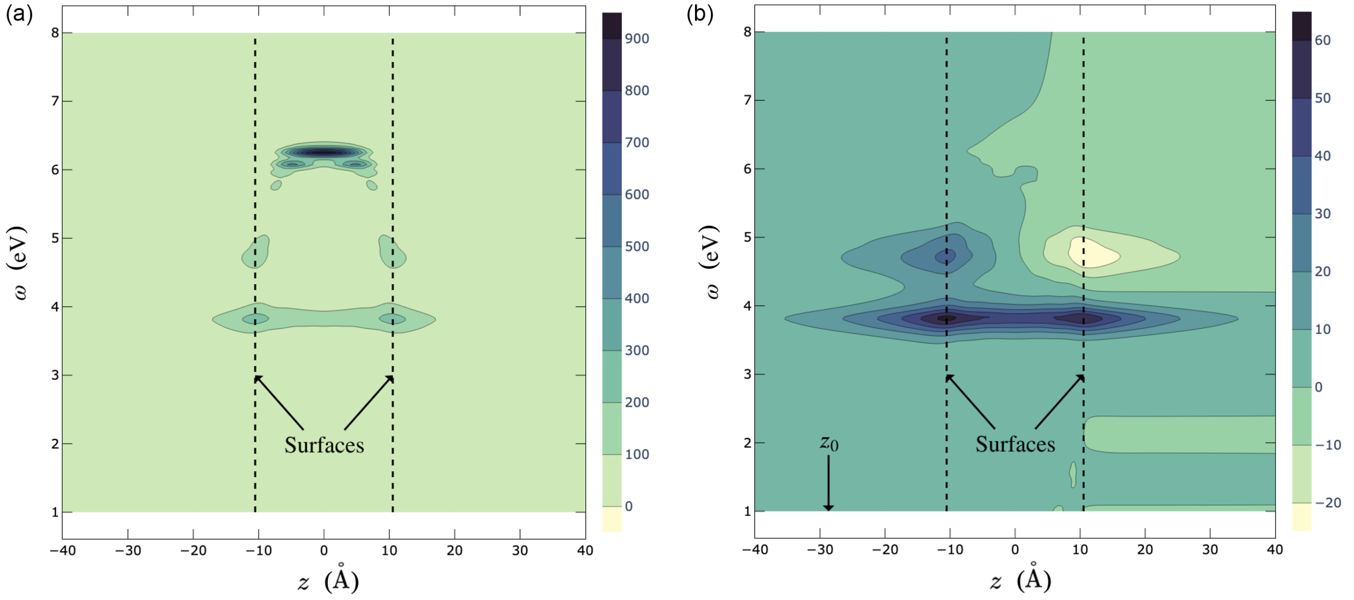

FIG. 4. (a) $\mathrm{Im}\,W(z,z;q_{||},\omega)$ for $q_{||}=0.076$ Å^{-1}. Two surface modes are visible: The symmetric one is at $\omega=3.83$ eV and the antisymmetric one at 4.71 eV. A bulk plasmon appears at 6.16 eV. (b) $\mathrm{Im}\,W(z_0,z;q_{||},\omega)$ for $z_0=-13.62$ Å and $q_{||}=0.076$ Å^{-1}. In this case, the symmetry of the surface-plasmon polariton (SPP) is clearly visible.

of the averaging associated with the macroscopic dielectric function. The relative weight of the bulk mode in the MLF dispersion is also found to increase for large $q_{//}$.

Additionally, the SCF approach leads to a lower relative intensity of the antisymmetric surface mode when compared with the NSCF one when using the SRF methodology. The comparison of Fig. 3 to the results gathered by Andersen *et al.* (see fig. 5 of Ref. [18]), for the same system but with first-principles methods, highlights the ability of the jellium model to identify the symmetric surface plasmon. However, the antisymmetric surface plasmon predicted in the jellium case is found to follow less closely the first-principles results and more closely the dielectric model in the long-wavelength (small $q_{||}$) regime (the first-principles results present a strong redshift, up to 1 eV, for the antisymmetric mode with respect to the classical and our jellium models). It is, however, expected that, in this limit, classical and quantum methods yield the same results. This redshift in the first-principles results probably comes from the smaller amount of vacuum between periodic replicas of the metallic film in the supercell approach in the first-principles calculations. In the jellium case, we found the symmetric mode harder to converge with respect to the amount of vacuum than the antisymmetric one. However, thanks to the smaller computational requirements, a better convergence with respect to this parameter can be performed for the two SPP modes in the jellium case.

In the short-wavelength regime (large $q_{||}$), on the other hand, nonlocal effects become significant, and the quantum results prevail. Our jellium calculations show the same $q_{||}^2$ dispersion as the one found in the first-principles data [18,83]. This highlights capabilities of the jellium model to correctly describe the quantum effects in both the long- and short-wavelength regimes, if the nonlocal effect associated with the atomistic description of the problem is not too important (which is not the case for Na).

Spatial information can be gleaned from the imaginary part of the screened interaction, as demonstrated in Fig. 4 for $q_{||}=0.076$ Å^{-1}. In the left part of the figure, the function is analyzed for a response at the perturbation location ($z=z'$), as suggested from the EELS theory. Although two surface modes are clearly observed at $\omega=3.83$ and 4.71 eV, along with a bulk plasmon at $\omega=6.18$ eV, the symmetries of the SPP modes cannot be resolved from the figure. This could be alleviated by setting the perturbation location on one side of the surface and analyzing the response over the whole range of positions ($z\neq z'$), as shown in the right part of Fig. 4 for $z_0=-13.62$ Å. In this case, the bulk mode is not excited, but the symmetry of the surface mode is revealed. The symmetric mode appears at 3.83 eV, while the response is antisymmetric for the 4.71 eV mode. Since it is more complex to extract all the relevant information from the screened interaction and it does not bring any added value, the following discussion will focus on the MLF and SRF.

Overall, these results underscore the interest of the jellium model and the possibility to obtain in-depth results by combining different methodologies. Even the very low intensity of the antisymmetric mode in the MLF helps to characterize its symmetry. Its importance will prevail even more when moving to more complex systems, when the visualization of the symmetries, thanks to the imaginary part of the screened interaction, will be more cumbersome to obtain.

B. Double slab

In this section, the analysis is extended to double-slab systems spaced by d_{gap}. They are composed of two jellium slabs equivalent to Na slabs of six atomic layers (12.6 Å), see Fig. 1(c). The dispersion curves are examined with respect to both d_{gap} and the parallel wave vector.

Before exploring the results for the jellium model, we introduce the classical results obtained by Richter and Geiger [84] for similar slab systems. For a layer of dielectric function ε_2 and thickness d_{gap} sandwiched between two layers of dielectric function ε_1 and thickness d_1, they obtained the following dispersion relation for the symmetric and antisymmetric surface modes [85]:

$$\varepsilon_1[(1+\varepsilon_1)\exp(q_{||}d_1)+(1-\varepsilon_1)\exp(-q_{||}d_1)]\tanh\left(\frac{q_{||}d_{\text{gap}}}{2}\right)+\varepsilon_2[(1+\varepsilon_1)\exp(q_{||}d_1)-(1-\varepsilon_1)\exp(-q_{||}d_1)]=0, \quad (38)$$

$$\varepsilon_1[(1+\varepsilon_1)\exp(q_{||}d_1)+(1-\varepsilon_1)\exp(-q_{||}d_1)]\coth\left(\frac{q_{||}d_{\text{gap}}}{2}\right)+\varepsilon_2[(1+\varepsilon_1)\exp(q_{||}d_1)-(1-\varepsilon_1)\exp(-q_{||}d_1)]=0. \quad (39)$$

In our case, $\varepsilon_2 = 1$ since vacuum separates the two slabs and $\varepsilon(\omega)$ is considered in the Drude approximation [Eq. (36)].

Figure 5 presents the evolution of the plasmonic modes as a function of the distance between the layer d_{gap} for $q_{||} = 0.076$ Å^{-1}. Classical (in the Drude approximation, $\omega_p =$ 6.1 eV) and jellium results present similar trends, with four distinctive surface modes merging two by two as d_{gap} increases. For large d_{gap}, i.e., when the slabs are well separated, the modes obviously akin to those in isolated slabs are recovered. Conversely, as d_{gap} decreases to 0, the excitations are those of a single slab with a doubled width with two surface modes at ≈4.1 and ≈4.5 eV and the bulk mode at 6.1 eV. Within an intermediate range of $d_{\text{gap}}(4-45$ Å), new surface modes emerge. They are particularly noticeable at small parallel wave vectors ($q_{||} < 0.25$ Å^{-1}), as will be analyzed afterward. For the time being, we continue the analysis for $q_{||} = 0.076$ Å^{-1}.

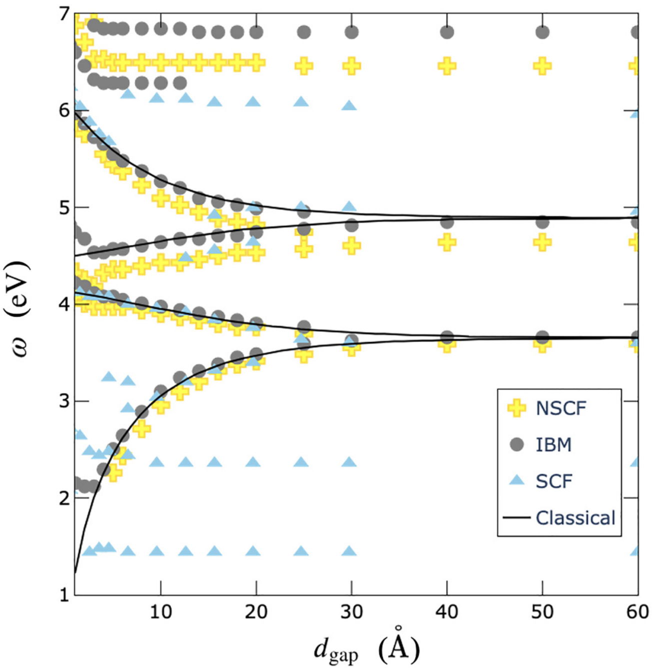

FIG. 5. Evolution of the plasmon frequency found in the self-consistent-field (SCF) case for the surface response function (SRF) in the double-slab system (each slab with a width of 12.6 Å) as the gap size is tuned. $q_{||} = 0.076$ Å^{-1}. The crosses represent the non-self-consistent-field (NSCF) case, the triangles the SCF case, and the dots the infinite barrier model (IBM) approximation (NSCF with $C = \infty$). The black lines correspond to the classical approximation where the Drude model is used for the dielectric function.

We note that the IBM model is the closest to the classical approximation. The NSCF model is globally redshifted by ~0.15 eV with respect to the latter (it can be seen in Fig. 1 that the density profiles for the single- and double-slab scenarios are different, implying that the tuning of the barrier height is no longer valid to reproduce the SCF results). Tuning the height of the barrier in the NSCF potential shows that, as its height decreases, the SPP frequencies are continuously redshifted. This can be linked to the ω_p value: As the size of the barrier is decreased, the electron gas is more spread, leading to a smaller average electronic density and, hence, to a smaller plasma frequency. The SCF model generally yields peaks close to the classical approximation. Nonetheless, some discrepancies can be found in the lower-energy mode and in the two higher-energy modes (the bulk modes are not analyzed here). In the former, the differences for very small gaps ($d_{\text{gap}} < 7$ Å) might be attributed to tunneling effects (in the NSCF case, the definition of the gap is more ambiguous as the parameter d becomes larger than d_{gap}, and so no conclusion could be made for d_{gap} <3 Å). In the two higher-energy modes, some peaks, below $d_{\text{gap}} = 12.61$ Å for the lowest one and between $d_{\text{gap}} = 4.54$ and 15.62 Å for the highest one, are not resolved, as they are hidden in the main SPP peak of the second-lowest energy mode. Some peaks between $d_{\text{gap}} = 12.61$ and 24.69 Å are also redshifted in the two higher-energy modes with respect to the classical approximation. Those are hence better reproduced by the NSCF model than by the IBM one. It is important to note that the redshift of the NSCF model does not impact the description of the modes, and the trends are still very similar in the SCF and NSCF cases. In the lowest part of the graph, one can observe two horizontal lines which are associated with weak electron-hole excitations. The rest of the discussion in this section is based on the SCF results.

The behavior for different parallel wave vectors is illustrated in Fig. 6. The figure displays a typical dispersion curve for two six-layer Na equivalent slabs with a gap of 9.82 Å for the classical dielectric approach and for the jellium model in the SRF-SCF approach. Four surface modes and one bulk mode are identified together with the electron-hole excitations. The bulk plasmons and the electron-hole excitations have very little weight and exhibit minimal deviations from the single-slab case, as expected.

For further characterization of the surface-plasmon modes, two types of symmetries are used in this analysis. As described previously, for one single slab, a plasmon mode can

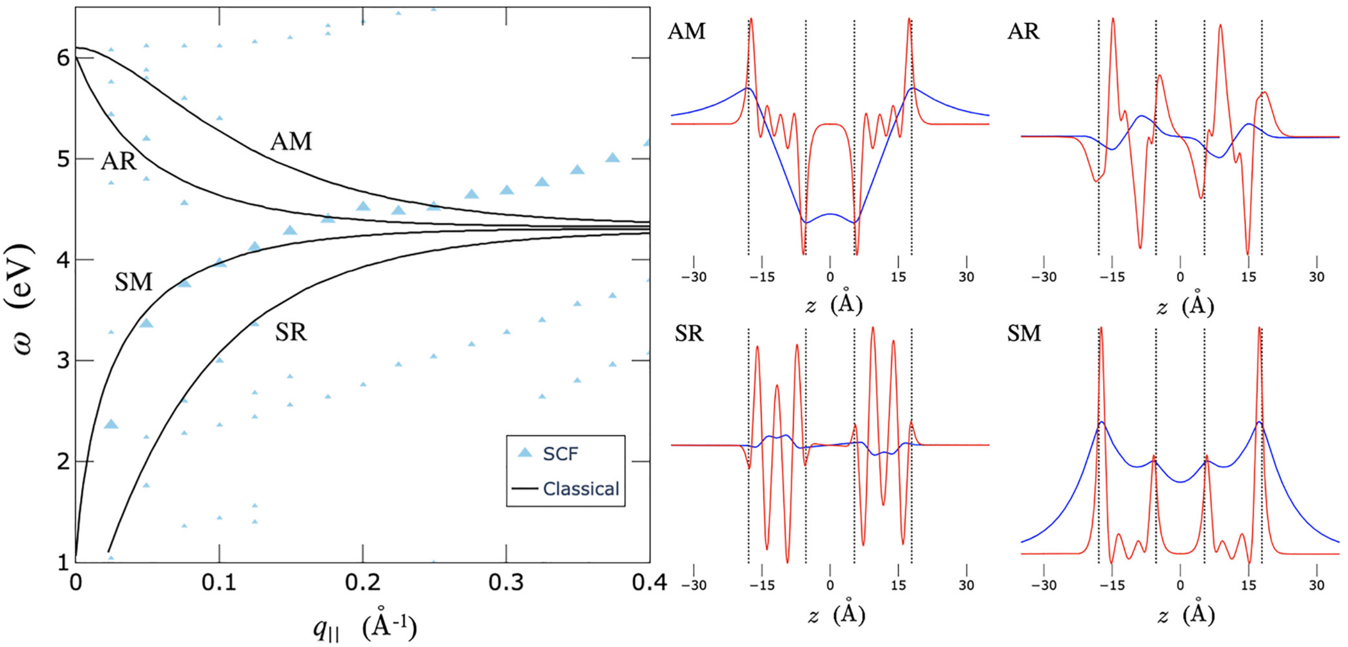

FIG. 6. Dispersion relation of the double symmetric six-atomic layer Na equivalent slab system with a gap of 9.82 Å using the surface response function (SRF). Left: In black, the prediction of the classical theory from Eqs. (38) and (39). In blue, the prediction from the self-consistent field (SCF). The size of the dots is proportional to the intensity of the mode (relative intensity for each $q_{||}$). Right: The four modes associated with each branch with the typical shape of the variation of, in red, the density $\rho_i(z)$ and, in blue, of the potential $V_i(z)$ associated with the mode. Top left is the antisymmetric mirrored (AM) mode, top right is the antisymmetric reversed (AR) mode, bottom left is the symmetric reversed (SR) mode, and bottom right is the symmetric mirrored (SM) mode. $q_{||} = 0.1$ Å^{-1} for the SR, SM, and AM modes, and $q_{||} = 0.75$ Å^{-1} for the AR mode.

be symmetric (S) or antisymmetric (A). Considering now one slab in interaction with another slab, such symmetry is broken, although it might hold approximately. Such a local symmetry will be called *inner symmetry*. By contrast, *global symmetry* is the true symmetry of the double-slab system, one slab being the mirror of the other. The modes will be labeled as mirror (M) ones when they are globally symmetric and reversed (R) ones when they are globally antisymmetric. The symmetry of each mode will be identified thanks to the density change obtained by the decomposition in the MLF (see the right panel of Fig. 6). As expected from the analysis of the single-slab case, reversed modes are found very weak in the MLF, as they are globally antisymmetric.

We examine now the left panel of Fig. 6. Starting from the lowest frequency, the branch labeled SR corresponds to a mode being inner symmetric and having a global antisymmetry from one slab to the other. The second branch SM corresponds to a (roughly) locally symmetric mode mirrored from one slab to the other (doubly symmetric). The third branch AR is an antisymmetric mode reversed, and the highest branch AM is an antisymmetric mode mirrored.

Comparing the dispersion curves computed here with the ones of the classical model, the general trends are similar, but the agreement is less good than for a single slab in the small wave vector regime. The SM and SR modes follow the classical approximation, while the AM mode is slightly blueshifted, and the AR mode is not well resolved. In the large wave vector regime, the same discrepancy is found as in the single-slab model where the four modes become degenerate because of the decoupling between the four surfaces in both approach. In the jellium model, a quadratic dispersion relation is observed, whereas the dispersion curve flattens in the classical case to tend toward $\omega_p/\sqrt{2}$.

Analyzing the predicted intensity of these modes reveals that the SM mode is the most intense, followed by the AR mode. The two remaining modes exhibit similar intensities, significantly lower than the AR mode. Comparing these observations with the classical case, it can be concluded that the SR- and AM-mode intensities are too small in the very small or very large gap regime to be observed, despite being still expected from the classical theory. Note, however, that this analysis might change if another response function characterizing a different experimental setup is used.

Finally, in anticipation of the case of two different slabs treated in the next section, it can be noted that the four modes still appear in the case where the two slabs do not have the same width (Fig. 7). The SM and SR modes do not present any significant changes in the resonant frequency when increasing the size of one of the two slabs by up to 3.18 Å, keeping the same $d_{\text{gap}} = 9.82$ Å. The AM and AR modes are still present but are redshifted by ∼0.2 eV when the size is increased by 3.18 Å, see Fig. 7.

C. Two different slabs

The case of two slabs made of different materials (i.e., with different densities) is now investigated. The following analysis considers only the NSCF model. As concerns the dielectric response, in the two previous sections, this NSCF model was seen not to differ fundamentally from the SCF one,

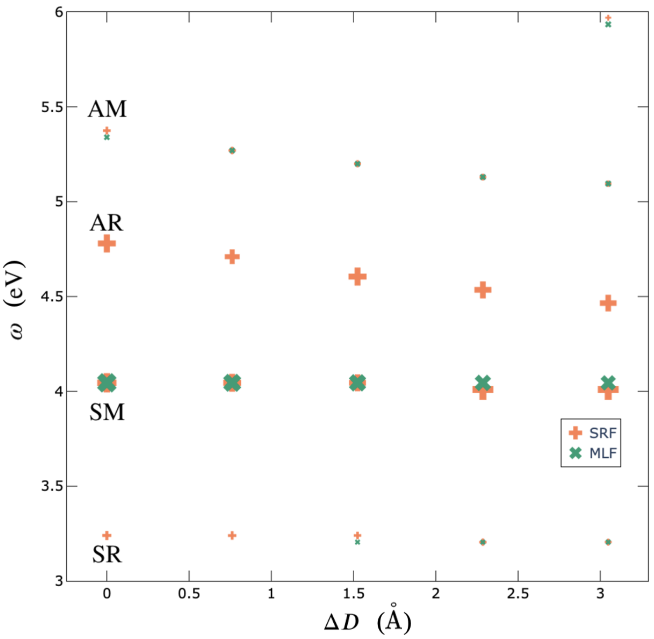

FIG. 7. Evolution of the surface mode frequency with respect to ΔD, the difference of width between the two slabs. The width of the left slab is fixed at 12.6 Å. The coral straight crosses present the results for the surface response function (SRF), while tilted green crosses show the results for the macroscopic loss function (MLF). The size of the symbols is proportional to the relative intensity of the peaks for a given ΔV.

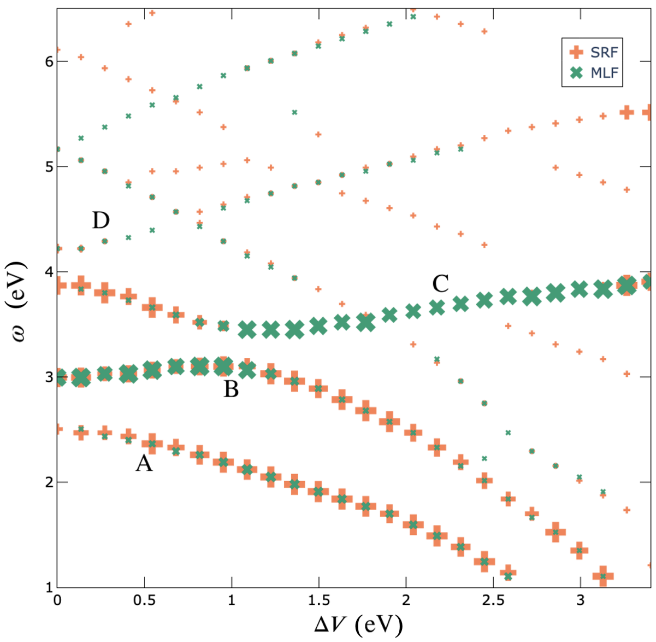

FIG. 8. Evolution of the plasmon modes for the two-different-slab system with respect to the difference of potential between the two wells in the non-self-consistent-field (NSCF) potential profile. The left well is kept at a fixed energy (-0.5 Ha, that is -13.61 eV, the vacuum being at 0 eV), while the right well is raised by ΔV. The coral straight crosses present the results for the surface response function (SRF), while tilted green crosses show the results for the macroscopic loss function (MLF). The size of the symbols is proportional to the relative intensity of the peaks for a given ΔV.

reproducing the trends and the principle modes accurately. Moreover, analyses of the trends are easier with the NSCF model, as the computation time is decreased since the SCF part is bypassed, while in our numerical investigations, we found the stabilization of the SCF ground state to be problematic in some cases.

The investigated systems are made of two slabs with a distance $d_{\mathrm{gap}} = 10.64$ Å with one of the wells deeper than the other. The total number of electrons in the system being kept constant and one of the wells being a preferential place for the electrons, an asymmetric repartition naturally arises. It results in slabs of two different materials that can then be defined by their electronic densities (not known beforehand), and since the neutrality is imposed, their background density can be computed *a posteriori*. The analysis will focus on the following aspects: The impact of the ratio of density between the two slabs and the dispersion relations obtained from the MLF and SRF.

Figure 8 presents the evolution of the surface plasmon gathered with the SRF when the electron density of the two slabs is tuned. The left-well depth is kept at -0.5 Ha, that is -13.61 eV, the vacuum being at 0 eV, while the right-well one is raised by ΔV with respect to the left well. The $\Delta V = 0$, leftmost value in the figure, corresponds therefore to identical slabs coupled. The parallel wave vector is set to 0.1 Å^{-1}.

The rightmost position shown corresponds to a case where the difference in energy is such that the left slab contains almost all the electrons, the right one being almost completely depleted. Figure 9 shows the correspondence between the ratio of electrons in the left slab and the total number of electrons in the system as a function of the difference of the potential. At ~6.5 eV, all the electrons have been transferred to states whose probability density is dominated by the left well.

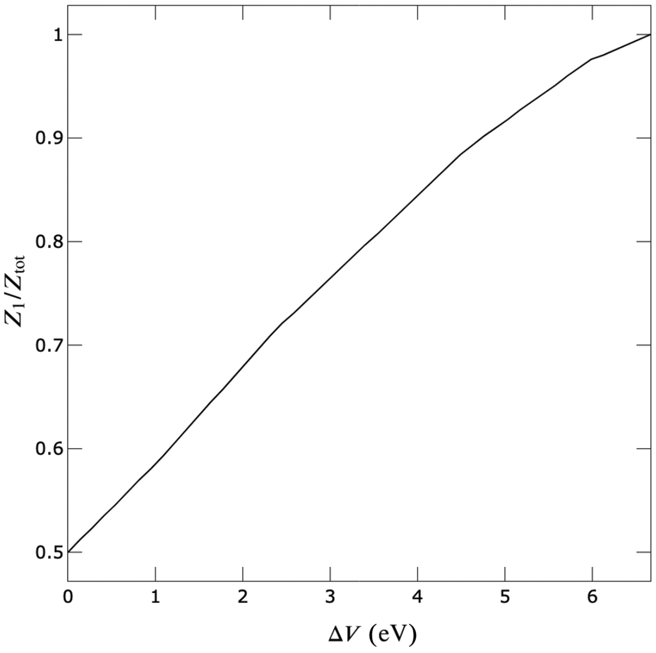

FIG. 9. Ratio of the amount of electrons in the left slab and the total amount of electrons in the system when ΔV is tuned.

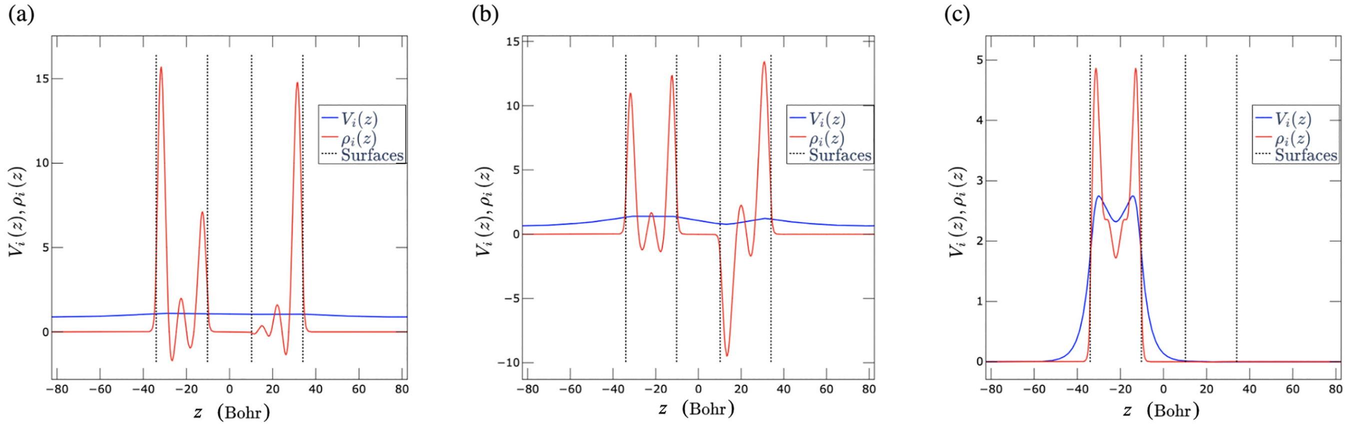

FIG. 10. Surface modes of branch (F) when $\Delta V = 0.41$ eV. (a) Example of a symmetric reversed (SR) mode for $q_{||} < 0.1$ Å^{-1}. (b) Example of a mode exhibiting symmetric-antisymmetric coupling at $0.1 < q_{||} < 0.3$ Å^{-1}. (c) Only the mode in the left slab is excited in branch (F) when $q_{||} > 0.3$ Å^{-1}.

The graph presented in Fig. 8 can be divided into three zones. In the first one, until $\Delta V \approx 0.5$ eV, the SPP modes can be seen as perturbations of the perfectly symmetric case. It is exemplified in Fig. 10(a) where the modes share similar characteristics with the SM mode of Fig. 6 with only the inner density peaks of the right slab being less pronounced. The second zone extends up to $\Delta V \approx 2$ eV. The difference in density compared with the symmetric case is more pronounced, presenting a coupling of one symmetric mode with one asymmetric mode to form the branches labeled (B) and (C). The resulting density is shown in Fig. 10(b). For the other two branches, labeled (A) and (D), the coupling between symmetric or antisymmetric modes is weaker. Finally, for $\Delta V > 2$ eV, the modes of the two slabs become strongly decoupled because the left slab has taken up >70% of the electron density. The frequencies of the modes of the right slab [(A) and (B) branches, Fig. 10(c)] then rapidly decrease as the electron density drops. Interestingly enough, the presence of a second slab makes the branch that starts with the SM mode, the branch (B), go up to reach a maximum at around $\Delta V = 0.82$ eV.

When looking in detail at the interplay between the modes, considering their spatial description, the situation where the two symmetric modes are coupled to form a SM mode, branch (B), is quickly (at about $\Delta V = 0.5$ eV) replaced by a situation where the antisymmetric mode of the right slab couples with the symmetric mode of the left slab (which contains more and more electrons as ΔV increases). After the maximum in (B), the spatial description shows a fading of the coupling, until the antisymmetric mode of the right slab is the only one excited. Branch (A), the one starting with the SR mode, presents a negative dispersion, and the symmetric mode of the right slab only couples lightly with the symmetric mode of the left slab.

The third branch, labeled (C), the one that starts with the AR mode and finishes at the position of the symmetric mode of the left slab, presents somehow the same features as the branch (B). The antisymmetric mode of the right slab is the main feature until the antisymmetric mode of the left slab finishes to be transformed in a symmetric mode. Then the latter becomes more and more the dominant mode until the antisymmetric mode of the right slab does not couple with it anymore. Finally, the upper branch, labeled (D), in the same way as branch (A), starts with the AM mode, but the antisymmetric mode of the left slab quickly becomes the leading mode, while the coupling with the antisymmetric mode of the right slab becomes less prevalent before fading completely when the density becomes almost null in this slab.

The dispersion relations for different values of ΔV are now analyzed (Fig. 11). Just as in the dispersion with respect to variation of the potential, we observe that the SPP modes evolve along well-defined branches. The possibility to couple or not with another plasmon mode makes the mode at the small wave vector very different from the one observed at the large wave vector of the same branch. Again, one can distinguish three zones in the dispersion relations: a first zone at long wavelength where the symmetries of the identical slabs case prevail; this zone becomes very narrow when ΔV increases. A second zone where the coupling between symmetric and antisymmetric modes are possible: This zone also shortens with the increase of ΔV. Finally, at very short wavelength, the modes are decoupled even for small differences of electronic density. We call these zones I, II, and III, respectively. From the comments made above, it is clear that, for $\Delta V > 2$ eV, the SPPs of two slabs are decoupled, and the dispersion curves are the superposition of the curves of the two isolated slabs.

Before this value, the densities are relatively close, allowing the SPPs of the two slabs taken separately to occur at similar energy, leading to a possible coupling. Figure 11 shows the dispersion curves for $\Delta V = 0.41$ eV (53.5–46.5% electron distribution) and $\Delta V = 1.36$ eV (62–38%).

In the $\Delta V = 0.41$ eV scenario, zone I goes up to $q_{||} \approx 0.06$ Å^{-1}, zone II finishes around $q_{||} \approx 0.3$ Å^{-1}, and zone III is everything above this value. Four main branches labeled (E)–(H) are distinguished in Fig. 11(a). In the MLF methodology, branches (G) and (H) merge with branch (F) around $q_{||} \approx 0.2$ Å^{-1}. In the SRF approach, branch (H) first merges with (G) and (F) at $q_{||} \approx 0.2$ Å^{-1}. They then merge altogether with branch (E) at $q_{||} \approx 0.3$ Å^{-1}.

As mentioned above, in zone I, the four modes are slight variations of the ones found in the symmetric case

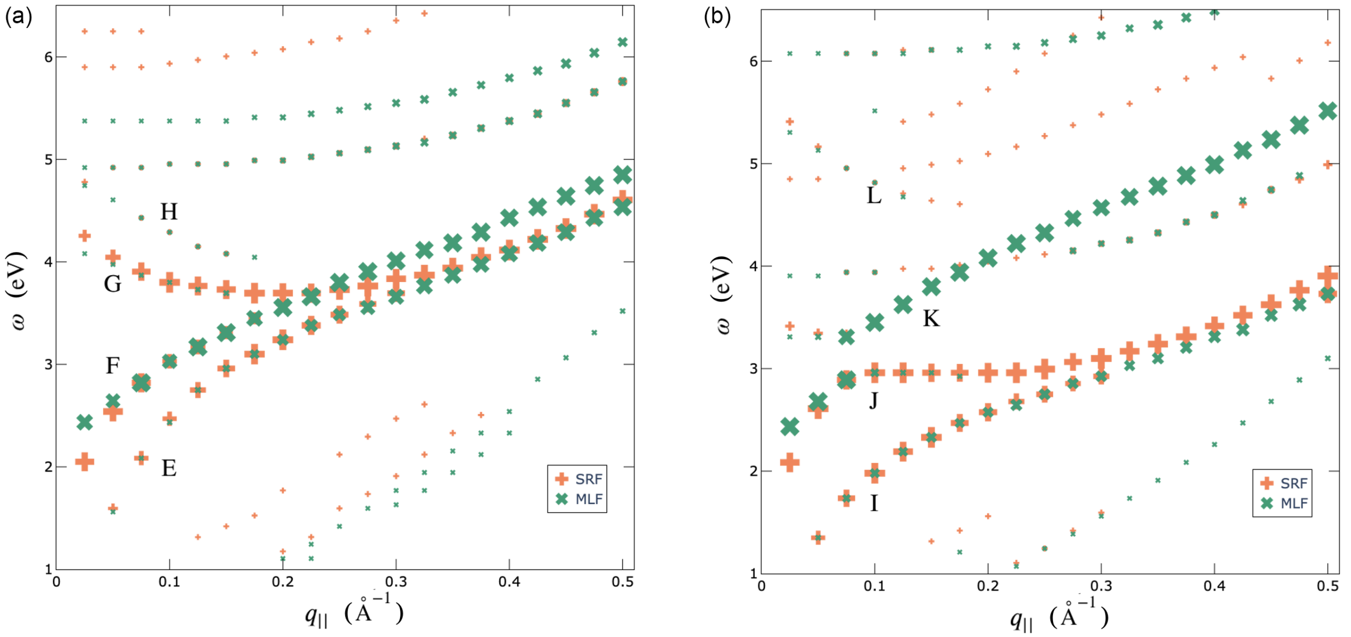

FIG. 11. Dispersion relation of the two-different-slabs system using the non-self-consistent-field (NSCF) approach with the results for the macroscopic loss function (MLF) in green and surface response function (SRF) in coral. (a) $\Delta V = 0.41$ eV case (53.5% of the electrons in the left slab). (b) $\Delta V = 1.36$ eV case (62% of the electrons in the left slab).

[see Fig. 10(a)], and the SRF and MLF approaches give the same results. As $q_{||}$ increases, some modes start to fade. In branch (E), it is the symmetric mode of the left slab. In branch (F), it is the symmetric mode of the right slab. In branches (G) and (H), it is the antisymmetric mode of the left and right slabs, respectively.

In zone II, branches (E) and (G) continue the transformation started in zone I. The fading modes are now almost negligible, and the SPP mode is driven by the symmetric mode of the right slab in branch (E) and the antisymmetric mode of the left slab in branch (H). In branch (G), the transformation continues. The antisymmetric mode of the left slab remains the same, while the antisymmetric mode of the left slab is transformed. The transformation affects primarily the rightmost part of the mode, gradually changing the sign of the variation from an increase of density to a decrease in the inner part of the slab. This transforms the mode from an antisymmetric mode to a symmetric one. Branch (G) corresponds to a symmetric antisymmetric coupling. Branch (F) presents a similar transformation. The symmetric mode of the right slab becomes antisymmetric as the variation of density on the innermost part of the slab gradually changes sign. The merge occurs when the two branches (F) and (G) have fully transited from their original coupling to a symmetric-antisymmetric coupling. In the MLF picture, this coupling remains after branches merge [even with branch (H) merging], but as $q_{||}$ increases, the antisymmetric mode starts fading. In the SRF picture, it is the symmetric mode that fades, leaving the antisymmetric mode the most prominent one before this branch merges with branch (E). This merge corresponds very similarly with what happens in the single-slab scenario where the energies of the antisymmetric and symmetric modes (of the right slab here) become degenerate. Hence, the symmetric mode prevails after the merge.

In zone III, branch (E) corresponds to the dispersion of the symmetric SPP of the right slab and branch (F) to the symmetric SPP of the left slab [shown in Fig. 10(c)]. Branch (F) is absent in the SRF methodology. The reason is that the SRF models a $z > 0$ electron trajectory so that the mode of the slab located in $z < 0$ has a vanishing weight. Note that, just as in the single-slab case, the antisymmetric mode is absent at short wavelength in both methodologies.

In the case where $\Delta V = 1.36$ eV, presented in Fig. 11(b), zones I and II are shorter, with their limits at $q_{||} \approx 0.02$ and 0.13 Å^{-1}, respectively. The analysis of the mode is relatively similar to the one of the case $\Delta V = 0.41$ eV. Again four branches are highlighted, labeled (I)–(L) in Fig. 11(b).

Branch (I) is equivalent to branch (E), the transition from the initial state to the final one as $q_{||}$ increases being faster in this case. Branch (L) is also like branch (H). The starting modes of branches (J) and (K) (SM and AR) quickly transition to a state of symmetric-antisymmetric coupling, but rather than merging in this case, they avoid crossing ($q_{||} = 0.04$ Å^{-1}), with the antisymmetric mode becoming the leading mode of branch (J), while the symmetric mode is more important in branch (K). Two distinct mergings occur then, one at $q_{||} = 0.13$ Å^{-1} between branches (K) and (L) and one at $q_{||} = 0.17$ Å^{-1}. Those merges are again equivalent to the ones of the single-slab case as the two slabs are decoupled. In Fig. 11(b), a branch starting at ∼3.90 eV can be observed. It corresponds to the bulk mode of the right slab. As the bulk mode does not produce an induced field large enough outside the slab, it cannot couple with the other slab. Finally, one can observe two differences between the SRF and MLF methodologies. The first one is the absence of branch (K) in the SRF approach, for the same reason as in $\Delta V = 0.41$ eV. Then the energy prediction for the mode of branch (I) is slightly blueshifted in the SRF approach with respect to the

MLF one. This results in a misidentification of the mode in the SRF scenario (as the identification is based on the MLF modes), where the leading mode is found to be antisymmetric, while a symmetric mode is expected in this short-wavelength regime. Convergence issues with respect to the grid sampling or vacuum size might be the cause for this, as the exponential in the integral of the SRF [Eq. (23)] can become quite important at large wave vector and large vacuum.

The analysis above, valid for jelliumlike systems such as alkaline metals or aluminum, shows the complexity of the interplay between different plasmonic modes. It also highlights the importance of the choice of the response function.

IV. CONCLUSIONS

In this paper, we have investigated the dielectric properties of jellium slabs, focusing on both single- and double-slab configurations. Through a combination of theoretical modeling and computational analysis, we have uncovered valuable insights into the behavior of surface modes and collective excitations in these systems. Our tool, available on Github [65], could be used to extend this analysis to many different systems.

Our analysis of single slabs revealed the impact of barrier height of the NSCF approach on the dispersion curves and loss functions. The right choice of this parameter can alleviate the need to use a self-consistent approach when the surface dielectric properties are considered in this single-slab case. The curves obtained from NSCF and SCF approaches for the symmetric and antisymmetric surface modes are very close to the ones of first-principles computations and even better in the long-wavelength regime where the size of the supercell is difficult to converge. We also highlight the failure of the macroscopic loss function to show the antisymmetric mode in symmetric systems in both NSCF and SCF approaches. Conversely, the surface response function presents all the modes.

Extending our investigation to two slabs introduces a new complexity, with the spacing between the slabs influencing the behavior of surface modes. We identify four distinct modes arising from interactions between symmetric slabs, shedding light on the interplay between surface-plasmon excitations in multilayered structures. In asymmetric slabs, coupling between modes of different symmetries is observed under certain constraints such as having densities not too different (here, this threshold is a variation of >0.02 Å^{-3} between the two slabs, but it depends on the SPP frequency of each material) and wave vectors small enough (this value depends on the difference of density).

These findings offer valuable insights for the design and characterization of nanoscale devices and materials, where surface plasmonics plays a crucial role in determining optical properties and device performance. Moreover, in this paper, we open avenues for future research, including the exploration of more complex excitations, the development of advanced modeling techniques, and the investigation of novel materials and geometries. Especially the search for coupling of plasmon modes in nanostructures of different materials is an interesting path.

In conclusion, in this paper, we contribute to the growing body of knowledge on surface plasmonics in jellium systems, offering valuable insights into their optical properties and paving the way for future advancements in nanophotonics and materials science.

ACKNOWLEDGMENTS

The authors acknowledge funding by the Federation Wallonia-Brussels through the ARC SURFASCOPE (UCLouvain-UNamur, Convention 19/24-102). This work is an outcome of the Shapeable 2D magnetoelectronics by design project (SHAPEme, Excellence of Science Project No. 560400077525) that has received funding from the Research Foundation–Flanders (FWO) and National Fund for Scientific Research (FRS-FNRS) under the Belgian Excellence of Science program. Computational resources have been provided by the supercomputing facilities of the Université catholique de Louvain and the Consortium des Equipements de Calcul Intensif en Fédération Wallonie Bruxelles funded by the FRS-FNRS under Grant No. 2.5020.11. V.L. thanks the FRS-FNRS for his Senior Research Associate position.

DATA AVAILABILITY

The data that support the findings in this paper are not publicly available. The data are available from the authors upon reasonable request.

[1] W. A. Murray and W. L. Barnes, Plasmonic materials, Adv. Mater. **19**, 3771 (2007).

[2] V. G. Kravets, A. V. Kabashin, W. L. Barnes, and A. N. Grigorenko, Plasmonic surface lattice resonances: A review of properties and applications, Chem. Rev. **118**, 5912 (2018).

[3] R. T. Hill, Plasmonic biosensors, WIREs Nanomed. Nanobiotechnol. **7**, 152 (2015).

[4] V. E. Ferry, J. N. Munday, and H. A. Atwater, Design considerations for plasmonic photovoltaics, Adv. Mater. **22**, 4794 (2010).

[5] B. Sharma, R. R. Frontiera, A.-I. Henry, E. Ringe, and R. P. Van Duyne, SERS: Materials, applications, and the future, Mater. Today **15**, 16 (2012).

[6] K. A. Willets and R. P. Van Duyne, Localized surface plasmon resonance spectroscopy and sensing, Annu. Rev. Phys. Chem. **58**, 267 (2007).

[7] P. L. Stiles, J. A. Dieringer, N. C. Shah, and R. P. Van Duyne, Surface-enhanced raman spectroscopy, Annu. Rev. Anal. Chem. **1**, 601 (2008).

[8] J. Langer *et al.*, Present and future of surface-enhanced Raman scattering, ACS Nano **14**, 28 (2020).

[9] F. Neubrech, C. Huck, K. Weber, A. Pucci, and H. Giessen, Surface-enhanced infrared spectroscopy using resonant nanoantennas, Chem. Rev. **117**, 5110 (2017).

[10] T. Colleu, A. Fekete, X. Gonze, A. Cloots, V. Liégeois, G.-M. Rignanese, and L. Henrard, Surface enhanced infrared

absorption mechanism and modification of the plasmonic response, J. Phys. Photon. **6**, 025003 (2024).
[11] W. L. Barnes, A. Dereux, and T. W. Ebbesen, Surface plasmon subwavelength optics, Nature (London) **424**, 824 (2003).
[12] A. N. Grigorenko, M. Polini, and K. S. Novoselov, Graphene plasmonics, Nat. Photon. **6**, 749 (2012).
[13] S. A. Maier, *Plasmonics: Fundamentals and Applications* (Springer, New York, 2007).
[14] R. H. Ritchie, Plasma losses by fast electrons in thin films, Phys. Rev. **106**, 874 (1957).
[15] A. Eguiluz, S. Ying, and J. Quinn, Influence of the electron density profile on surface plasmons in a hydrodynamic model, Phys. Rev. B **11**, 2118 (1975).
[16] A. G. Eguiluz, The electron-plasmon interaction near a metal surface, Solid State Commun. **33**, 21 (1980).
[17] A. G. Eguiluz, Screening near a metal surface: Plasmon effects, Phys. Rev. B **23**, 1542 (1981).
[18] K. Andersen, K. W. Jacobsen, and K. S. Thygesen, Spatially resolved quantum plasmon modes in metallic nano-films from first-principles, Phys. Rev. B **86**, 245129 (2012).
[19] R. A. Ferrell, Characteristic energy loss of electrons passing through metal foils. II. Dispersion relation and short wavelength cutoff for plasma oscillations, Phys. Rev. **107**, 450 (1957).
[20] C. Powell and J. Swan, Origin of the characteristic electron energy losses in aluminum, Phys. Rev. **115**, 869 (1959).
[21] E. Economou, Surface plasmons in thin films, Phys. Rev. **182**, 539 (1969).
[22] D. Newns, Dielectric response of a semi-infinite degenerate electron gas, Phys. Rev. B **1**, 3304 (1970).
[23] M. Chen and J. Bolton, Retarded dielectric theory of electron energy loss in multilayers and superlattices, Superlattices Microstruct. **12**, 531 (1992).
[24] J. F. Dobson, Electron-gas boundary properties in non-neutral jellium (wide-parabolic-quantum-well) systems, Phys. Rev. B **46**, 10163 (1992).
[25] J. M. Pitarke, V. M. Silkin, E. V. Chulkov, and P. M. Echenique, Theory of surface plasmons and surface-plasmon polaritons, Rep. Prog. Phys. **70**, 1 (2007).
[26] P. Koval, F. Marchesin, D. Foerster, and D. Sánchez-Portal, Optical response of silver clusters and their hollow shells from linear-response TDDFT, J. Phys.: Condens. Matter **28**, 214001 (2016).
[27] J. T. Titantah and M. Karttunen, *Ab initio* calculations of optical properties of silver clusters: Cross-over from molecular to nanoscale behavior, Eur. Phys. J. B **89**, 125 (2016).
[28] M. Kuisma, A. Sakko, T. P. Rossi, A. H. Larsen, J. Enkovaara, L. Lehtovaara, and T. T. Rantala, Localized surface plasmon resonance in silver nanoparticles: Atomistic first-principles time-dependent density-functional theory calculations, Phys. Rev. B **91**, 115431 (2015).
[29] M. Manninen, Structures of small alkali-metal clusters, Phys. Rev. B **34**, 6886 (1986).
[30] N. D. Lang and W. Kohn, Theory of metal surfaces: Charge density and surface energy, Phys. Rev. B **1**, 4555 (1970).
[31] N. D. Lang and W. Kohn, Theory of metal surfaces: Work function, Phys. Rev. B **3**, 1215 (1971).
[32] N. G. Asmar and E. G. Gwinn, Jellium surfaces in Al$_x$Ga$_{1-x}$As heterostructures, Phys. Rev. B **46**, 4752 (1992).
[33] W. Ekardt, Dynamical polarizability of small metal particles: Self-consistent spherical jellium background model, Phys. Rev. Lett. **52**, 1925 (1984).
[34] J. M. Pitarke and A. G. Eguiluz, Jellium surface energy beyond the local-density approximation: Self-consistent-field calculations, Phys. Rev. B **63**, 045116 (2001).
[35] A. Liebsch, *Electronic Excitations at Metal Surfaces* (Springer, New York, 1997).
[36] J. F. Dobson and J. Wang, Testing the local density approximation with energy-versus-separation curves of jellium slab pairs, Phys. Rev. B **69**, 235104 (2004).
[37] A. R. Echarri, E. J. H. Skjølstrup, T. G. Pedersen, and F. J. G. de Abajo, Theory of electron energy-loss spectroscopy in atomically thin metallic films, Phys. Rev. Res. **2**, 023096 (2020).
[38] M. Rocca, L. Yibing, F. B. de Mongeot, and U. Valbusa, Surface plasmon dispersion and damping on Ag(111), Phys. Rev. B **52**, 14947 (1995).
[39] R. Ritchie and A. Marusak, The surface plasmon dispersion relation for an electron gas, Surf. Sci. **4**, 234 (1966).
[40] R. Vincent and J. Silcox, Dispersion of radiative surface plasmons in aluminum films by electron scattering, Phys. Rev. Lett. **31**, 1487 (1973).
[41] K.-D. Tsuei, E. Plummer, A. Liebsch, E. Pehlke, K. Kempa, and P. Bakshi, The normal modes at the surface of simple metals, Surf. Sci. **247**, 302 (1991).
[42] Z. Penzar and M. Sunjic, Surface electronic response in the random phase approximation and infinite barrier model: Surface plasmons, electron-hole pairs and the interaction with external particles, Phys. Scr. **30**, 431 (1984).
[43] B. N. J. Persson and E. Zaremba, Electron-hole pair production at metal surfaces, Phys. Rev. B **31**, 1863 (1985).
[44] A. García-Lekue and J. M. Pitarke, Energy loss of charged particles interacting with simple metal surfaces, Phys. Rev. B **64**, 035423 (2001).
[45] F. Schulte, A theory of thin metal films: Electron density, potentials and work function, Surf. Sci. **55**, 427 (1976).
[46] J. F. Dobson, Plasmons on wide epitaxially-grown quantum wells, Aust. J. Phys. **46**, 391 (1993).
[47] W. L. Schaich and J. F. Dobson, Excitation modes of neutral jellium slabs, Phys. Rev. B **49**, 14700 (1994).
[48] V. M. Silkin, E. V. Chulkov, and P. M. Echenique, Band structure versus dynamical exchange-correlation effects in surface plasmon energy and damping: A first-principles calculation, Phys. Rev. Lett. **93**, 176801 (2004).
[49] V. M. Silkin, T. Nagao, V. Despoja, J. P. Echeverry, S. V. Eremeev, E. V. Chulkov, and P. M. Echenique, Low-energy plasmons in quantum-well and surface states of metallic thin films, Phys. Rev. B **84**, 165416 (2011).
[50] N. Tancogne-Dejean, C. Giorgetti, and V. Véniard, Optical properties of surfaces with supercell *ab initio* calculations: Local-field effects, Phys. Rev. B **92**, 245308 (2015).
[51] C. Giorgetti, I. Iagupov, and V. Véniard, Electron energy loss spectroscopy of thin slabs with supercell calculations, Phys. Rev. B **101**, 035431 (2020).
[52] V. Despoja, P. M. Echenique, and M. Šunjić, Nonlocal microscopic theory of quantum friction between parallel metallic slabs, Phys. Rev. B **83**, 205424 (2011).
[53] V. Despoja, L. Marušić, and M. Šunjić, Excitation spectra of coupled metallic slabs, Solid State Commun. **140**, 270 (2006).

[54] P. J. Feibelman, Exact microscopic theory of surface contributions to the reflectivity of a jellium solid, Phys. Rev. B **14**, 762 (1976).

[55] N. A. Mortensen, Mesoscopic electrodynamics at metal surfaces—From quantum-corrected hydrodynamics to microscopic surface-response formalism, Nanophotonics **10**, 2563 (2021).

[56] T. V. Teperik, P. Nordlander, J. Aizpurua, and A. G. Borisov, Robust subnanometric plasmon ruler by rescaling of the nonlocal optical response, Phys. Rev. Lett. **110**, 263901 (2013).

[57] T. Christensen, W. Yan, A.-P. Jauho, M. Soljačić, and N. A. Mortensen, Quantum corrections in nanoplasmonics: Shape, scale, and material, Phys. Rev. Lett. **118**, 157402 (2017).

[58] Y. Luo, A. I. Fernandez-Dominguez, A. Wiener, S. A. Maier, and J. B. Pendry, Surface plasmons and nonlocality: A simple model, Phys. Rev. Lett. **111**, 093901 (2013).

[59] W. Yan, M. Wubs, and N. Asger Mortensen, Projected dipole model for quantum plasmonics, Phys. Rev. Lett. **115**, 137403 (2015).

[60] P. Gonçalves, T. Christensen, N. Rivera, A.-P. Jauho, N. A. Mortensen, and M. Soljačić, Plasmon-emitter interactions at the nanoscale, Nat. Commun. **11**, 366 (2020).

[61] V. Karanikolas, I. Thanopulos, J. D. Cox, T. Kuroda, J.-I. Inoue, N. A. Mortensen, E. Paspalakis, and C. Tserkezis, Quantum surface effects in strong coupling dynamics, Phys. Rev. B **104**, L201405 (2021).

[62] A. Babaze, E. Ogando, P. Elli Stamatopoulou, C. Tserkezis, N. Asger Mortensen, J. Aizpurua, A. G. Borisov, and R. Esteban, Quantum surface effects in the electromagnetic coupling between a quantum emitter and a plasmonic nanoantenna: Time-dependent density functional theory vs. semiclassical Feibelman approach, Opt. Express **30**, 21159 (2022).

[63] W. Zhu, R. Esteban, A. G. Borisov, J. J. Baumberg, P. Nordlander, H. J. Lezec, J. Aizpurua, and K. B. Crozier, Quantum mechanical effects in plasmonic structures with subnanometre gaps, Nat. Commun. **7**, 11495 (2016).

[64] G. Toscano, J. Straubel, A. Kwiatkowski, C. Rockstuhl, F. Evers, H. Xu, N. Asger Mortensen, and M. Wubs, Resonance shifts and spill-out effects in self-consistent hydrodynamic nanoplasmonics, Nat. Commun. **6**, 7132 (2015).

[65] A. Cloots, 1D potential solver to obtain dielectric properties of 2D periodic jellium. Available at https://github.com/gitacloots/1d_systems. Moreover, in addition to the source code, specific data that were used to produce the figures are available from the authors upon reasonable request.

[66] G. Giuliani and G. Vignale, *Quantum Theory of the Electron Liquid* (Cambridge University Press, Cambridge, 2008).

[67] In SI units, the plasma frequency is defined as $\omega_{\rm p}^2 = e^2 n_{\rm e}/(\varepsilon_0 m_0)$, where e is the electron charge, ε_0 the vacuum permittivity, and m_0 the electron mass.

[68] V. Despoja, L. Marušić, and M. Šunjić, Surface spectral functions and excitation frequencies in thin metallic films, Fizika A **14**, 207 (2005).

[69] X. Gonze, Towards a potential-based conjugate gradient algorithm for order-N self-consistent total energy calculations, Phys. Rev. B **54**, 4383 (1996).

[70] A. G. Eguiluz, Self-consistent static-density-response function of a metal surface in density-functional theory, Phys. Rev. B **31**, 3303 (1985).

[71] Thanks to the periodicity of the problem, the response functions, usually expressed as functions of $\mathbf{r}$ and $\mathbf{r}'$, are here described by a vector $q_{||}$ invariant rotationally in the plane x-y and two spatial coordinates z, z'. To go from the former to the latter, a 2D Fourier transform must be performed on the x-y coordinates.

[72] The sum over $k_{||}$ can be replaced by a factor $2A(\epsilon_{\rm f} - \epsilon_l)/(2\pi)$.

[73] The screened interaction being computed from Eq. (22), the response can be analyzed over the whole space, not only for z, z' pairs far from the surface as suggested by Eq. (24).

[74] The simple Fourier transform is defined for a quantity $\alpha(z, z', q_{||}, \omega)$ as $\alpha_G(q_{||}, z', \omega) = 1/L \int \exp[-i(q_{||} + G)z]\alpha(z, z', q_{||}, \omega))dz$, while the double Fourier transform of a quantity $\beta(z, z', q_{||}, \omega)$ is defined as $\beta_{G,G'}(q_{||}, \omega) = 1/L^2 \iint \exp[-i(q + G)z]\beta(z, z', q_{||}, \omega) \exp[i(q_{||} + G')z']dzdz'$.

[75] Here, the supercell formalism is used, as the computation time is reasonably small. Nonetheless, if the systems should be larger, we encourage the use of a truncated Coulomb potential. This note is particularly important if one wants to go to beyond jellium.

[76] B. Majérus, E. Guillaume, P. Kockaert, and L. Henrard, Anisotropy and effective medium approach in the optical response of two-dimensional material heterostructures, Phys. Rev. B **108**, 245412 (2023).

[77] The intensities can be compared in normalized spectra $l_{\rm slab}(\omega)$ with $l_{\rm slab}(\omega) = l_{\rm M}(\omega)\frac{d_{\rm vac}}{d_{\rm cell}}$, were $d_{\rm vac}$ and $d_{\rm cell}$ are the width of the vacuum and of the total cell (vacuum and jellium), respectively.

[78] J. Friedel, XIV. The distribution of electrons round impurities in monovalent metals, London, Edinburgh Dublin Philos. Mag. J. Sci. **43**, 153 (1952).

[79] E. P. Wigner and J. Bardeen, Theory of the work functions of monovalent metals, in *Part I: Physical Chemistry. Part II: Solid State Physics: The Collected Works of Eugene Paul Wigner*: Vol. A/4, edited by A. S. Wightman (Springer, Berlin, 1997), pp. 398–401.

[80] N. Ashcroft and N. Mermin, *Solid State Physics* (Saunders, Philadelphia, 1976).

[81] A. R. Echarri, P. Gonçalves, C. Tserkezis, F. J. G. de Abajo, N. A. Mortensen, and J. D. Cox, Optical response of noble metal nanostructures: Quantum surface effects in crystallographic facets, Optica **8**, 710 (2021).

[82] C. Ciracì and F. Della Sala, Quantum hydrodynamic theory for plasmonics: Impact of the electron density tail, Phys. Rev. B **93**, 205405 (2016).

[83] In the paper of Echarri *et al.* [37], the dispersion curves do not show this trend; however, we believe they did not sufficiently inspect short wavelengths for it to appear, as they limit their study to wave vectors >0.1 Å^{-1}.

[84] H. Richter and J. Geiger, Energy losses of fast electrons in multi-layer systems, Z. Phys. B **42**, 39 (1981).

[85] The symbols used for the hyperbolic tangent and cotangent function in the original paper are misleading: The tan and cot symbols should be replaced by tanh and coth, respectively.